

SÍGAME SIMULATIONS OF THE [C II], [O I] AND [O III] LINE EMISSION FROM STAR FORMING GALAXIES AT $Z \simeq 6$

KAREN OLSEN,¹ THOMAS R. GREVE,² DESIKA NARAYANAN,³ ROBERT THOMPSON,⁴ ROMEEL DAVÉ,^{5,6,7} LUIS NIEBLA RIOS,¹ AND STEPHANIE STAWINSKI¹

¹*School of Earth and Space Exploration, Arizona State University, 781 S Terrace Rd, Tempe, AZ 85287, USA*

²*Department of Physics and Astronomy, University College London, Gower Street, London WC1E 6BT, UK*

³*Department of Astronomy, University of Florida, 211 Bryant Space Sciences Center, Gainesville, FL, USA*

⁴*Portalarium, Austin, TX 78731, USA*

⁵*University of the Western Cape, Bellville, Cape Town 7535, South Africa*

⁶*South African Astronomical Observatory, Observatory, Cape Town 7925, South Africa*

⁷*Institute for Astronomy, Royal Observatory, Edinburgh EH9 3HJ, UK*

ABSTRACT

Of the almost 40 star forming galaxies at $z \gtrsim 5$ (not counting QSOs) observed in [C II] to date, nearly half are either very faint in [C II], or not detected at all, and fall well below expectations based on locally derived relations between star formation rate and [C II] luminosity. This has raised questions as to how reliable [C II] is as a tracer of star formation activity at these epochs and how factors such as metallicity might affect the [C II] emission. Combining cosmological zoom simulations of galaxies with SÍGAME (Simulator of Galaxy Millimeter/submillimeter Emission) we have modeled the multi-phased interstellar medium (ISM) and its emission in [C II], as well as [O I] and [O III], from 30 main sequence galaxies at $z \simeq 6$ with star formation rates $\sim 3 - 23 \text{ M}_\odot \text{ yr}^{-1}$, stellar masses $\sim (0.7 - 8) \times 10^9 \text{ M}_\odot$, and metallicities $\sim (0.1 - 0.4) \times Z_\odot$. The simulations are able to reproduce the aforementioned [C II]-faintness of some normal star forming galaxies sources at $z \geq 5$. In terms of [O I] and [O III] very few observations are available at $z \gtrsim 5$ – but our simulations match two of the three existing $z \gtrsim 5$ detections of [O III], and are furthermore roughly consistent with the [O I] and [O III] luminosity relations with star formation rate observed for local starburst galaxies. We find that the [C II] emission is dominated by the diffuse ionized gas phase and molecular clouds, which on average contribute $\sim 66\%$ and $\sim 27\%$, respectively. The molecular gas, which constitutes only $\sim 10\%$ of the total gas mass is thus a more efficient emitter of [C II] than the ionized gas, which makes up $\sim 85\%$ of the total gas mass. A principal component analysis shows that the [C II] luminosity correlates with the star formation activity of a galaxy as well as its average metallicity. The low metallicities of our simulations together with their low molecular gas mass fractions can account for their [C II]-faintness, and we suggest these factors may also be responsible for the [C II]-faint normal galaxies observed at these early epochs.

Keywords: cosmology: theory – galaxies: high-redshift – galaxies: ISM – line: formation – methods: numerical – submillimeter: ISM

1. INTRODUCTION

The far-IR fine-structure transitions $[\text{C II}] \ ^2P_{3/2} - ^2P_{1/2}$ at $157.7 \mu\text{m}$, $[\text{OI}] \ ^3P_2 - ^3P_1$ at $63.2 \mu\text{m}$, and $[\text{O III}] \ ^3P_1 - ^3P_0$ at $88.4 \mu\text{m}$ (hereafter referred to as $[\text{C II}]$, $[\text{OI}]$, and $[\text{O III}]$) have been used as diagnostic tracers of the interstellar medium (ISM) and star formation activity for over two decades (e.g., [Malhotra et al. 1997](#); [Luhman et al. 1998](#); [Fischer et al. 1999](#); [Luhman et al. 2003](#); [Sturm et al. 2010](#); [Stacey et al. 2010](#); [Ferkinhoff et al. 2010](#); [Wang et al. 2013b](#); [De Looze et al. 2014](#); [Pineda et al. 2014](#); [Sargsyan et al. 2014](#); [Rigopoulou et al. 2014](#); [Capak et al. 2015](#); [Gullberg et al. 2015](#); [Willott et al. 2015](#); [Díaz-Santos et al. 2013](#); [Díaz-Santos et al. 2017](#)). $[\text{C II}]$ is often observed to be one of the strongest emission lines in the spectra of galaxies, and can comprise up to $\sim 0.1 - 1\%$ of the infrared (IR) luminosity ([Stacey et al. 1991](#); [Helou et al. 2001](#)). With C^0 having an ionization potential of only 11.3 eV and with the $[\text{C II}]$ line having an upper state energy of $E_u/k_B \sim 91 \text{ K}$, several ISM phases can contribute to its emission. It is an important coolant in diffuse H I clouds, diffuse ionized gas, and even molecular gas, where its critical density spans a wide range from $\sim 5 \text{ cm}^{-3}$ for collisions with electrons at $T_k = 8000 \text{ K}$ to $\sim 7.6 \times 10^3 \text{ cm}^{-3}$ for collisions with molecules at $T_k = 20 \text{ K}$ ([Goldsmith et al. 2012](#)). In photo-dissociation regions (PDR), it is associated with both the interface layer of atomic gas, as well as from the ionized gas in the H II region itself (e.g., [Stacey et al. 1991](#); [Malhotra et al. 2001](#); [Brauhar et al. 2008](#); [Smith et al. 2017](#)). $[\text{OI}]$ has a critical density of $\sim 4.7 \times 10^5 \text{ cm}^{-3}$ and an upper state energy of $E_u/k_B \sim 228 \text{ K}$, which makes it an efficient tracer of PDRs. Since the ionization potential of O^+ is 35.1 eV , $[\text{O III}]$ is seen in hot diffuse ionized gas (e.g., H II regions or the hot ionized medium), where the transition is easily excited ($n_{\text{cr}} \sim 5.1 \times 10^2 \text{ cm}^{-3}$ and $E_u/k_B \sim 163 \text{ K}$).

Although they trace different ISM phases, all three fine-structure lines have been proposed as tracers of the star formation rate (SFR) of galaxies ([Kapala et al. 2015](#); [Herrera-Camus et al. 2015](#)). For example, [De Looze et al. \(2014\)](#) found the line emissions to correlate with the SFRs for a sample of local and high- z starburst galaxies. However, the same study also found that for local metal-poor dwarfs, $[\text{OI}]$ and $[\text{O III}]$ were better at predicting the SFR than $[\text{C II}]$, which showed an increased scatter and a somewhat shallower correlation ([De Looze et al. 2014](#)). Furthermore, local (ultra) luminous IR galaxies ((U)LIRGs) show a significant decrement in their $[\text{C II}]$ luminosity (e.g., [Malhotra et al. 2001](#)). Self-absorption of the $[\text{OI}]$ line due to intervening cold or subthermally excited gas has also been reported in (U)LIRGs (e.g. [Rosenberg et al. 2015](#)) possibly de-

creasing the line strength and its ability to trace the star formation.

At redshifts > 5 , $[\text{C II}]$ has been detected in little more than a dozen normal star forming galaxies ([Capak et al. 2015](#); [Gullberg et al. 2015](#); [Willott et al. 2015](#); [Knudsen et al. 2016](#); [Pentericci et al. 2016](#); [Bradač et al. 2017](#); [Decarli et al. 2017](#); [Smit et al. 2017](#)), and about the same number of non-detections (i.e., upper limits). The non-detections, and a small number of detections, predominantly have very low $L_{[\text{C II}]}/\text{SFR}$ ratios and do not appear to form a $[\text{C II}]$ -SFR sequence with the remaining $[\text{C II}]$ -detected galaxies ([Kanekar et al. 2013](#); [Ouchi et al. 2013](#); [González-López et al. 2014](#); [Ota et al. 2014](#); [Schaerer et al. 2015](#); [Maiolino et al. 2015](#); [Inoue et al. 2016](#)). Proposed explanations for the low $[\text{C II}]$ emission include: low metallicities and thus C abundance; strong stellar feedback disrupting the neutral ISM from which most $[\text{C II}]$ emission is expected to arise ([Maiolino et al. 2015](#); [Inoue et al. 2016](#); [Pentericci et al. 2016](#); [Bradač et al. 2017](#)); extreme UV-fields and thus a high ionization parameter $\langle U \rangle^1$ ([Willott et al. 2015](#)). An increase in $\langle U \rangle$ leads to higher grain charges (and grain temperatures) causing a deficiency of the photo-electrons available to heat the gas and hence a reduced photoelectric heating efficiency. Additionally, the effects of stellar age have been invoked ([González-López et al. 2014](#); [Schaerer et al. 2015](#)) and different (possibly much denser) photodissociation region (PDR) structures than seen locally ([Ouchi et al. 2013](#); [Ota et al. 2014](#)).

With the low number of $[\text{OI}]$ and $[\text{O III}]$ detections at high redshift, it is practically impossible to establish an $[\text{OI}]$ -SFR or $[\text{O III}]$ -SFR relation for the high redshift ($0.5 < z < 6.6$) sample of [De Looze et al. \(2014\)](#). Since that study, two $\text{Ly}\alpha$ emitters (LAEs) at $z = 7.2120$ and 8.38 , and a normal star forming galaxy at $z = 7.1$ have been detected in $[\text{O III}]$ ([Inoue et al. 2016](#); [Laporte et al. 2017](#); [Carniani et al. 2017](#)).

Galaxy-scale simulations have been developed that attempt to account for the observations of the above fine-structure lines, in particular, how their emissions are linked to the ISM phases and to global galaxy properties, such as metallicity, star formation efficiency, ionization parameter, dust mass fraction, compactness and phase filling factors (e.g., [Cormier et al. 2012](#); [Vallini et al. 2013](#); [Olsen et al. 2015](#); [Accurso et al. 2017](#); [Katz et al. 2017](#)). By combining codes of stellar population synthesis, radiative transfer, photoionization, and astrochemistry into simulations of starburst regions, [Accurso et al. \(2017\)](#) found that the increases in the specific star

¹ Number of far-UV photons per hydrogen atom

formation rate of a galaxy leads to a decrease in the fraction of the [C II] emission coming from the molecular gas phase, due to stronger UV radiation fields which will tend to shrink the molecular regions. Applied to local normal galaxies, their code predicts that as much as 60 – 80% of the [C II] emission emerges from the molecular gas. Cormier et al. (2012) utilized the photoionisation code CLOUDY (Ferland et al. 2013) to model a number of FIR fine-structure line emissions (including [C II], [O I], and [O III]) from the multi-phased ISM in the starburst low-metallicity galaxy Haro 11. They found that PDRs account for only 10 % of the [C II] emission, with the remaining emission arising in the diffuse ionized medium, but a larger PDR contribution when lowering the density or including magnetic fields.

Some simulation studies have focused specifically on $z \gtrsim 6$ galaxies using either cosmological simulations (Vallini et al. 2013, 2015; Pallottini et al. 2017) or an analytical framework (Muñoz & Furlanetto 2014; Bonato et al. 2014; Popping et al. 2016; Narayanan & Krumholz 2017). Simulating galaxies at $z \approx 6.6$, Vallini et al. (2015) parametrises their [C II] luminosities as a function of SFR and metallicity. They find that the [C II]-faint sources at these epochs are explained by either low metallicity or negative feedback from regions of intense star formation. They also find that the [C II] budget is dominated by emission from PDRs, with < 10% coming from the diffuse neutral gas. Pallottini et al. (2017) calculated the [C II] emission from a multi-phase ISM in a normal star forming galaxy at $z \simeq 6$ by combining abundance calculations using CLOUDY with the method of inferring the [C II] emission by Vallini et al. (2013, 2015) and applying it to a cosmological simulation. They too were able to reproduce the underluminous [C II] sources found at this epoch and, just like Vallini et al. (2015) attributed it to low metallicity. They also find that while $\sim 95\%$ of the total [C II] luminosity is coming from the main gas disk of the galaxy, about 30% of the total C⁺ mass is situated in an outflow. Owing to the low density of the outflow, however, this mass does not contribute significantly to the total [C II] luminosity.

In this paper we simulate the [C II], [O I] and [O III] line emission from normal star forming galaxies at $z \simeq 6$, although the emphasis of our analysis will be on [C II]. Due to the different origins of the lines, a multi-phased modelling of the ISM is required. To this end we have combined the output from cosmological zoom simulations of normal star forming galaxies at this epoch with an updated version of SÍGAME (SÍmulator of GALaxy Millimeter/submillimeter Emission; Olsen et al. 2015). §2 describes the simulation codes used for the galaxy evolution and the galaxy sample chosen for our study. The

sub-grid modelling of the ISM is done with SÍGAME and is described in §3. The simulation results are presented, analyzed and discussed in §4 and §5, respectively, followed by our conclusions in §6. Throughout, we adopt a flat cold dark matter (Λ CDM) cosmology with cosmological parameters; $\Omega_\Lambda = 0.7$, $\Omega_M = 0.3$ and $h = 0.68$ (Planck Collaboration et al. 2016).

2. COSMOLOGICAL GALAXY FORMATION SIMULATIONS

We use cosmological zoom simulations of galaxies extracted from the MUFASA cosmological simulation (Davé et al. 2016, 2017), utilizing the same feedback prescription as in MUFASA. We first briefly summarize the zoom technique, then discuss the particulars of the MUFASA simulations.

The zoom technique is summarized in recent reviews (e.g. Somerville & Davé 2015), hence we only condense the salient details here. We begin by simulating a dark matter-only $50h^{-1} \text{ Mpc}^3$ volume utilizing GIZMO², which employs the GADGET-2 tree-particle-mesh gravity solver (Springel 2005). This is run at fairly low resolution, with 512^3 particles resulting in a particle mass of $m_{\text{DM}} = 7.8 \times 10^8 h^{-1} M_\odot$, from $z = 249$ to $z = 0$ with the aim of simulating a population of dark matter halos to be re-simulated (with baryons) at much higher mass resolution. The initial conditions are generated with MUSIC (Hahn & Abel 2011), and have the exact same random seeds as the cosmological MUFASA simulation with gas dynamics.

At $z = 2$, we identify a randomly-selected set of halos within the mass range $\sim (0.4 - 3) \times 10^{13} M_\odot$ for re-simulation at higher resolution, now including baryons. We build an elliptical mask around each halo extending to $2.5\times$ the distance of the farthest dark matter particle from the center of the halo, and define this as the Lagrangian high-resolution region to be re-simulated. We seed this region with higher-resolution dark matter ($m_{\text{DM}} = 1 \times 10^6 h^{-1} M_\odot$) and gas ($1.9 \times 10^5 h^{-1} M_\odot$) fluid elements, and resimulate. We employ adaptive gravitational softening of all particles throughout the simulation (Hopkins 2015), with minimum force softening lengths of 12, 3 and 3 pc for dark matter, gas and stars respectively.

The hydrodynamic simulations are run with a modified version of the N -body/hydrodynamics solver, GIZMO (Hopkins 2015) using the meshless finite mass (MFM) hydrodynamics solver. MFM uses a Riemann solver to compute pressure gradients, whose solution is obtained

² <http://www.tapir.caltech.edu/~phopkins/Site/GIZMO.html>

in a frame chosen to conserve mass within each mesh cell. This retains essential advantages of mesh methods that handle shocks and contact discontinuities accurately, along with that of particle-based methods in which mass can be tracked and followed.

These simulations utilize the suite of physics developed for the MUFASA cosmological simulations as described in [Davé et al. \(2016, 2017\)](#). We refer the reader to these papers for more detail, and summarize the relevant details here. Star formation occurs only in dense molecular gas, where the H_2 gas fraction (f_{H_2}) is determined based on the [Krumholz et al. \(2009\)](#) and [Krumholz & Gnedin \(2011\)](#) relations that approximate the molecular gas mass fraction as a function of the gas phase metallicity and surface density. Due to our high resolution, we assume no clumping on scales below our resolution limit. Star formation follows a volumetric [Schmidt \(1959\)](#) relation with an imposed star formation efficiency of $\sigma_* = 0.02$.

Young stars generate winds using a decoupled, two-phase wind. These winds have a probability for ejection that is a fraction of the star formation rate probability, according to the best-fit relation from the Feedback in Realistic Environments simulations studied (FIRE) by [Muratov et al. \(2015\)](#) (and is additionally motivated by analytic arguments; [Hayward & Smith 2015](#)). The ejection velocity scales with the galaxy circular velocity again following the [Muratov et al. \(2015\)](#) scaling relations. These winds are decoupled from hydrodynamic forces or cooling until either its relative velocity to the background gas is less than half the local sound speed; the wind reaches a density limit less than $0.01\times$ that of the critical density of star formation, or at least 2% of the Hubble time has elapsed since the time of launch.

Feedback from longer-lived stars (i.e. Asymptotic Giant Branch stars and Type Ia supernovae) is also included. These delayed feedback sources follow [Bruzual & Charlot \(2003\)](#) tracks with a [Chabrier \(2003\)](#) initial mass function, and deposit heavy metals (H, He, C, N, O, Ne, Mg, Si, S, Ca, and Fe) into the interstellar medium. The chemical enrichment yields for Type II SNe, Type Ia SNe and AGB stars are taken from [Nomoto et al. \(2006\)](#); [Iwamoto et al. \(1999\)](#) and [Oppenheimer & Davé \(2008\)](#) parameterisations respectively.

We extract model galaxies from snapshots at $5.875 < z < 6.125$ with stellar masses (M_*) and SFRs in the range $\sim (0.7 - 8) \times 10^9 M_\odot$ and $\sim 3 - 23 M_\odot \text{yr}^{-1}$, respectively. In total, we select 30 galaxies, hereafter named G1, ..., G30 by order of increasing stellar mass. Fig. 1 shows the locations of G1, ..., G30 in the SFR– M_* diagram. The galaxies are consistent with the observational determination of the $z \sim 6$ main sequence (MS) of

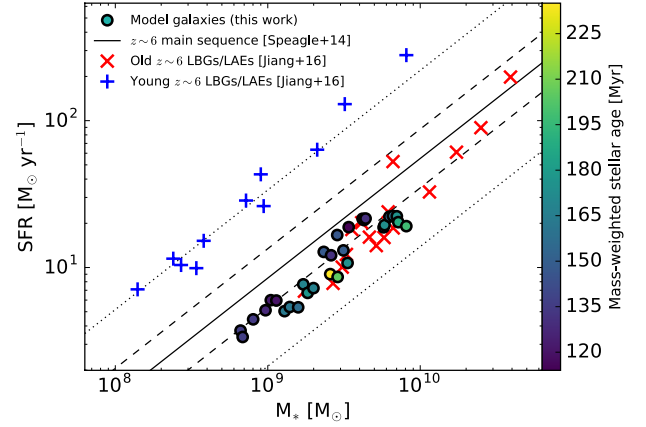


Figure 1. SFR vs. M_* for our 30 simulated galaxies (filled circles, color-coded according to their stellar mass weighted average ages). The observed SFR – M_* relation at $z \simeq 6$ as determined by [Speagle et al. \(2014\)](#) is shown as a solid line accompanied by dashed and dotted lines indicating the 1σ and 3σ scatter around the relation, respectively. For comparison we show the positions of $z \sim 6$ “old” (> 100 Myr) and “young” (< 30 Myr) LBGs/LAEs [Jiang et al. \(2016\)](#).

star forming galaxies by [Speagle et al. \(2014\)](#), although slightly offset towards higher M_* for a given SFR. Also shown in Fig. 1 are the $z \sim 6$ LBGs and LAEs studied by [Jiang et al. \(2016\)](#) who divided their sample into “old” (> 100 Myr) and “young” (< 30 Myr) galaxies, depending upon their stellar age as derived from spectral energy distribution (SED) fitting. As the color-coding shows, our model galaxies are consistent in terms of M_* , SFR and stellar age with the “old” LBG/LAE population ([Jiang et al. 2016](#)). Table 1 gives an overview of other global parameters of our simulations that are relevant for this study. The SFR of each galaxy was calculated as a mean over the past 100 Myr (mass of new stars created over the past 100 Myr divided by 100 Myr) and the radius of the disk is calculated by the analysis software CAESAR³, an extension of the YT simulation tools⁴, using a friends-of-friends algorithm. Table 1 also lists the average metallicity of each simulated galaxy, which is calculated as the SFR-weighted average over all the fluid elements. These SFR-weighted average metallicities, $\langle Z \rangle_{\text{SFR}}$, range from 14% to 45% of the solar metallicity.

3. SÍGAME

³ <https://bitbucket.org/rthompson/caesar>

⁴ <http://yt-project.org/>

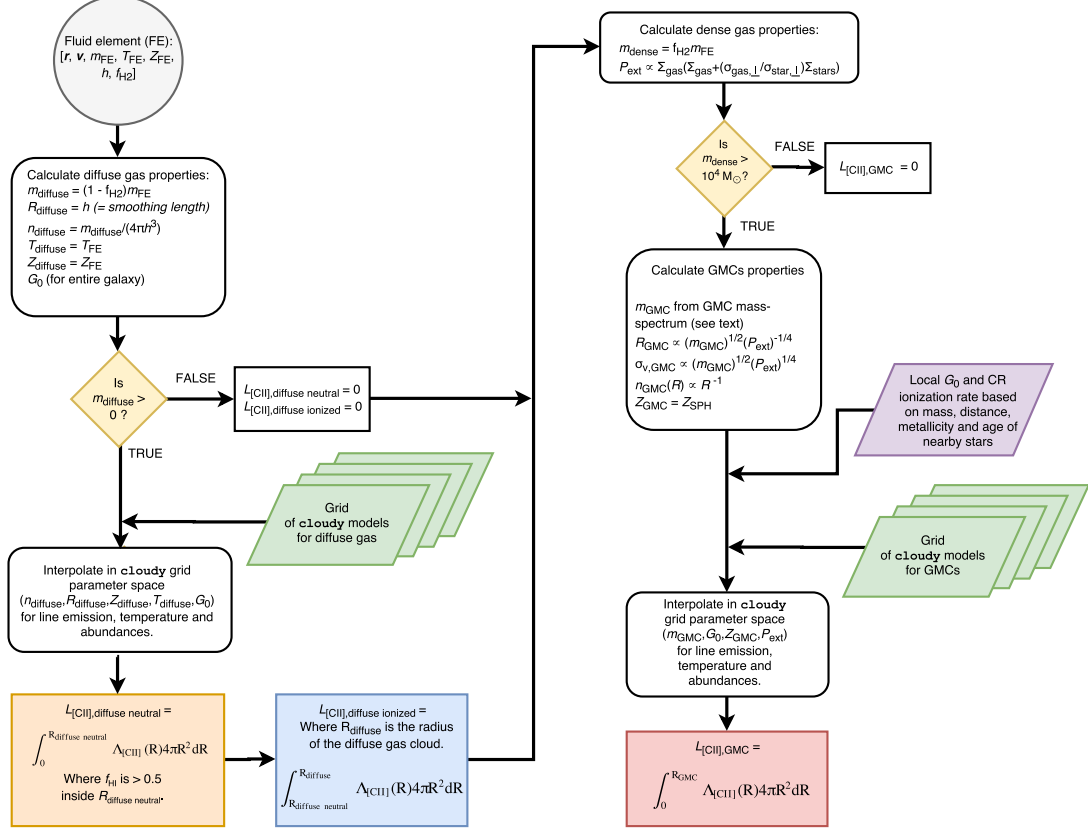


Figure 2. Flowchart of the subgridding procedures applied by SÍGAME to each gas fluid element in the MUFASA simulations.

For the purposes of this paper we have updated SÍGAME from the version presented in Olsen et al. (2015). The main updates are: a more sophisticated calculation of the UV radiation fields, and the implementation of CLOUDY⁵ ver. 17 Ferland et al. (2017). Below we describe in detail the updates made. Fig. 2 illustrates how a gas fluid element is processed in this updated version of SÍGAME.

3.1. Dense phase

SÍGAME uses a method described in Rahmati et al. (2013) to derive the dense gas mass fraction, f_{H_2} , associated with a given fluid element. The dense gas mass is then $m_{dense} = m_{gas} f_{H_2}$, where m_{gas} is the total gas mass of the fluid element. The dense gas is divided into giant molecular clouds (GMCs) by randomly sampling the Galactic GMC mass spectrum over the mass range $10^4 - 10^6 M_\odot$ until the remaining dense gas mass is $< 10^4 M_\odot$ at which point the gas is discarded. If the initial m_{dense} does not exceed this lower limit no GMCs are associated with the fluid element and m_{dense} is set

to zero. No more than 0.01 % of the dense gas mass in any of our 30 simulations are discarded during this process. The Galactic GMC mass spectrum adopted here has a power law slope of 1.8 as derived by Blitz et al. (2007) for the outer MW. In §5 we explore the effects of adopting a shallower as well as a steeper spectrum.

Each GMC inherits the metallicity, Z , of its parent fluid element, and is subjected to an external cloud pressure, P_{ext} , which is calculated from the surface densities of stars and star-forming gas as well as their vertical velocity dispersions using an assumption of hydrostatic mid-plane equilibrium (see Olsen et al. 2015). The GMC sizes (R_{GMC}) are derived from a pressure-normalized mass-size relation (Olsen et al. 2015), which results in cloud radii in the range 5.8 to 43.6 pc (Fig. 3). The GMC radial density profiles are assumed to follow a truncated logotropic profile:

$$n_H(R) = n_{H,ext} \left(\frac{R_{GMC}}{R} \right), \quad (1)$$

where $n_H(R > R_{GMC}) = 0$ and the external density, $n_{H,ext}$, is 2/3 of the average density within R_{GMC} . The GMCs are randomly distributed within $0.5 \times$ the smoothing length of the fluid element.

⁵ <http://www.nublado.org/>

Table 1. Global properties of the 30 simulated $z \simeq 6$ galaxies used for this work.

Name	z	$R_{\text{gal}}^{\text{a}}$ [kpc]	M_{\star} [$10^9 M_{\odot}$]	M_{gas} [$10^9 M_{\odot}$]	SFR ^b [$M_{\odot} \text{ yr}^{-1}$]	$\langle Z \rangle_{\text{SFR}}^{\text{c}}$ [Z_{\odot}]	$\frac{M_{\text{GMC}}}{M_{\text{gas}}}$	$\frac{M_{\text{diffuse neutral}}}{M_{\text{gas}}}$	$\frac{M_{\text{diffuse ionized}}}{M_{\text{gas}}}$
G1	6.12	9.34	0.663	11.493	3.720	0.186	0.071	0.059	0.869
G2	6.25	7.45	0.684	8.170	3.365	0.136	0.093	0.063	0.844
G3	6.00	8.12	0.802	11.810	4.437	0.178	0.089	0.077	0.833
G4	5.88	9.67	0.967	11.821	5.118	0.183	0.075	0.054	0.871
G5	5.88	8.86	1.047	13.016	5.991	0.170	0.140	0.099	0.761
G6	5.75	7.49	1.138	10.259	5.959	0.152	0.115	0.090	0.794
G7	6.00	9.25	1.289	11.499	5.045	0.156	0.089	0.079	0.831
G8	6.12	11.29	1.393	14.489	5.384	0.155	0.088	0.064	0.847
G9	6.25	8.31	1.583	9.170	5.358	0.198	0.143	0.059	0.797
G10	6.25	5.70	1.710	9.532	7.681	0.159	0.216	0.030	0.754
G11	5.75	12.68	1.826	16.511	6.719	0.236	0.063	0.054	0.882
G12	5.88	11.37	1.994	15.293	7.239	0.211	0.020	0.119	0.861
G13	6.12	7.41	2.329	10.718	12.776	0.208	0.107	0.022	0.871
G14	5.75	11.05	2.569	14.296	9.014	0.231	0.103	0.062	0.835
G15	6.00	9.07	2.603	12.520	12.115	0.242	0.053	0.107	0.840
G16	6.00	7.70	2.856	11.051	16.644	0.202	0.180	0.022	0.798
G17	5.88	6.67	2.873	8.119	8.625	0.258	0.214	0.070	0.716
G18	5.75	13.84	3.134	19.713	13.078	0.217	0.020	0.090	0.889
G19	6.12	10.46	3.338	10.771	10.739	0.282	0.023	0.129	0.848
G20	6.25	7.78	3.395	10.299	18.833	0.334	0.021	0.025	0.954
G21	6.00	4.15	4.186	7.822	21.474	0.412	0.072	0.032	0.896
G22	6.12	6.40	4.277	9.044	21.042	0.452	0.020	0.033	0.947
G23	6.25	6.70	4.381	10.061	21.558	0.339	0.031	0.028	0.941
G24	6.25	7.47	5.750	11.261	18.776	0.293	0.157	0.014	0.828
G25	5.88	7.03	5.833	9.567	19.442	0.354	0.039	0.038	0.923
G26	6.12	10.43	6.278	14.223	22.182	0.371	0.138	0.056	0.805
G27	6.00	10.84	6.622	13.159	22.455	0.370	0.103	0.052	0.844
G28	5.88	10.52	7.024	9.680	22.332	0.425	0.139	0.046	0.815
G29	5.75	7.38	7.178	6.710	20.364	0.392	0.201	0.013	0.785
G30	5.75	6.48	8.104	9.095	19.128	0.409	0.039	0.030	0.931

^a R_{gal} is the radius defined by the group finder **CAESAR** together with the yt project (see text).

^bThe SFR has been averaged over the past 100 Myr.

^c $\langle Z \rangle_{\text{SFR}}$ is the average of the SFR-weighted metallicities, in units of solar metallicity, of the fluid elements belonging to a galaxy.

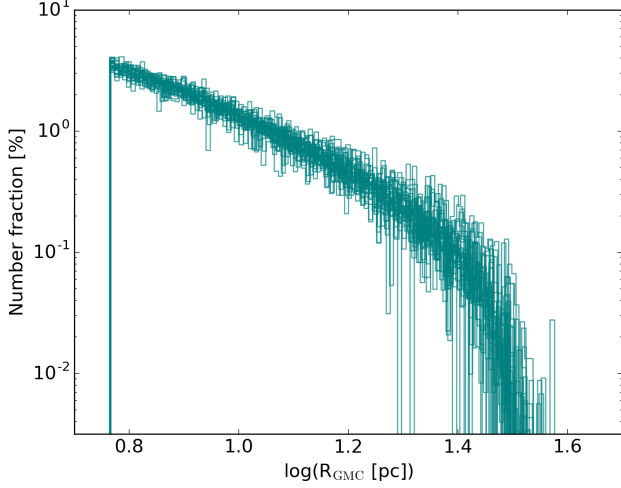


Figure 3. The distributions of cloud radii for the GMC populations in our 30 model galaxies.

Each GMC is assumed to be isotropically irradiated by a local FUV radiation field from nearby young stars and a constant diffuse background FUV field from the overall stellar population of the galaxy. The local field is the cumulative FUV radiation field from stellar particles within one smoothing length of the gas fluid element position (\mathbf{r}_{gas}). Each contribution is scaled according to the stellar mass ($m_{*,i}$) and distance ($|\mathbf{r}_{\text{gas}} - \mathbf{r}_{*,i}|$) from the gas element such that the strength of the local field is given by:

$$\frac{G_{0,\text{loc}}}{\text{erg cm}^{-2} \text{s}^{-1}} = \sum_{|\mathbf{r}_{\text{gas}} - \mathbf{r}_{*,i}| < h} \frac{L_{\text{FUV},i}}{4\pi |\mathbf{r}_{\text{gas}} - \mathbf{r}_{*,i}|^2} \frac{m_{*,i}}{10^4 M_{\odot}} \quad (2)$$

where $|\mathbf{r}_{\text{gas}} - \mathbf{r}_{*,i}|$ is in cm and $m_{*,i}$ is in M_{\odot} . $L_{\text{FUV},i}$ is the FUV luminosity in units of erg s^{-1} of a $10^4 M_{\odot}$ stellar population with a metallicity and age as that of the i th stellar particle. The $L_{\text{FUV},i}$ -values are found by interpolating over a grid of *starburst99*⁶ (Leitherer et al. 2014) stellar population models of mass $10^4 M_{\odot}$ and covering the range of metallicities and ages of the stellar populations encountered in the simulations. These models adopt a Kroupa initial mass function (IMF) and an instantaneous burst star formation history. We note that the hydrodynamic simulations use a slightly different IMF (Chabrier), but expect the differences in UV luminosity to be negligible. The strength of the constant background FUV field is set to:

$$\frac{G_{0,\text{bg}}}{\text{erg cm}^{-2} \text{s}^{-1}} = G_{0,\text{MW}} \frac{\Sigma_{\text{SFR}}}{\Sigma_{\text{SFR,MW}}}, \quad (3)$$

⁶ <http://www.stsci.edu/science/starburst99/>

where $G_{0,\text{MW}} = 9.6 \times 10^{-4} \text{ erg cm}^{-2} \text{s}^{-1}$ ($= 0.6$ Habing) is the Galactic FUV field flux (Seon et al. 2011), and Σ_{SFR} and $\Sigma_{\text{SFR,MW}}$ are the average SFR surface densities of the model galaxy in question and the MW, respectively. Σ_{SFR} is defined as the total SFR divided by the area of the galaxy disk seen face-on, using the radii listed in Table 1. Our model galaxies span a range in Σ_{SFR} from 0.013 to $0.40 M_{\odot} \text{ yr}^{-1} \text{ kpc}^{-2}$, which corresponds to $4 - 120 \times \Sigma_{\text{SFR,MW}}$ since $\Sigma_{\text{SFR,MW}} \simeq 0.003 M_{\odot} \text{ yr}^{-1}$. The latter is calculated using a SFR of $1.9 M_{\odot} \text{ yr}^{-1}$ (Chomiuk & Povich 2011) and a radius of 13.5 kpc for the star forming disk of the MW (Kennicutt & Evans 2012).

The total FUV flux impinging on a GMC is $G_{0,\text{GMC}} = G_{0,\text{loc}} + G_{0,\text{bg}}$. For the sake of simplicity we assume that the spectral shape of this FUV field is identical to that of the standard FUV background in the Solar neighborhood (the "ism" table in CLOUDY).

Cosmic rays (CRs) can be an important source of heating and ionization in dense clouds (Papadopoulos et al. 2011, 2014), and are therefore included in the treatment of GMCs in SÍGAME. Each GMC is subjected to a CR ionization rate, which is given by:

$$\frac{\zeta_{\text{CR,GMC}}}{\text{s}^{-1}} = \zeta_{\text{CR,MW}} \frac{G_{0,\text{GMC}}}{G_{0,\text{MW}}}, \quad (4)$$

where $\zeta_{\text{CR,MW}} = 3 \times 10^{-17} \text{ s}^{-1}$ is the average CR ionization rate in the MW (e.g., Webber 1998).

The distributions of m_{GMC} , $G_{0,\text{GMC}}$, Z and P_{ext} for the GMC populations in our simulations are shown in Fig. 4. Once the GMCs have been configured in the above described manner, CLOUDY is used to calculate the ionization states, thermal state and line cooling rates throughout the clouds. The line luminosities of a GMC is calculated as the line cooling rates provided by CLOUDY integrated over the volume of the cloud.

3.2. Diffuse phase

The diffuse gas mass associated with a fluid element is $m_{\text{diffuse}} = m_{\text{gas}} - m_{\text{dense}}$. Provided $m_{\text{diffuse}} > 0$ for the fluid element in question, the diffuse gas is distributed evenly within a spherical region with a radius equal to the smoothing length of the fluid element and centered on its position. Furthermore, the diffuse gas inherits the metallicity and temperature of the fluid element. Fig. 5 shows the distributions of densities, radii, metallicities, and temperatures for the diffuse clouds in our model galaxies.

The clouds of diffuse gas are larger (typical radii are $\sim 1 \text{ kpc}$ but span the range $0.1 - 5 \text{ kpc}$) than the dense

gas clouds and have lower densities (typical densities are $\sim 10^{-2} \text{ cm}^{-3}$ but span the range $\sim 10^{-4} - 10^2 \text{ cm}^{-3}$). It is assumed that the diffuse clouds are unassociated with star formation sites and, as a result, they are only irradiated (isotropically) by the diffuse background FUV field (i.e., $G_{0,\text{bg}}$). The heating and ionization of the diffuse gas is also affected by the presence of CRs, and we set the CR ionization rate felt by the diffuse phase to:

$$\frac{\zeta_{\text{CR,bg}}}{s^{-1}} = \zeta_{\text{CR,MW}} \frac{G_{0,\text{bg}}}{G_{0,\text{MW}}}. \quad (5)$$

As done for the GMCs, CLOUDY is used to calculate the ionization states and line cooling rates throughout the diffuse clouds. **SÍGAME** uses the output from CLOUDY to define the transition from the inner neutral to the outer ionized regions of the diffuse clouds: the radius where the neutral hydrogen fraction, i.e., the number density of H I divided by the number density of H I and H II, is 0.5. In cases where this fraction is > 0.5 at all radii, **SÍGAME** identifies the entire cloud as diffuse neutral gas. The above procedure allows us to operate with a diffuse neutral and a diffuse ionized gas phase in our simulations, in addition to the dense gas phase. The line luminosities of the neutral and ionized phases within a cloud are calculated by integrating the line cooling rates over the volumes of each of the two phases.

3.3. CLOUDY model setup

The main input parameters for CLOUDY in this work are the cloud radius, the radial density profile of the cloud, the FUV spectrum impinging on the cloud, the element abundances, and the gas kinetic temperature. In the following we describe how each of these parameters are specified for GMCs and diffuse gas clouds.

Cloud radius: For our GMC models, the external pressure is used together with the GMC mass to determine the cloud radius (see §3.1), whereas the diffuse clouds have sizes given by the smoothing length of the parent fluid element.

Density profile: The mass and radius is combined to derive the density profile of each GMC (eq. 1), while the diffuse gas clouds are assigned uniform densities (§3.2).

FUV radiation field: The GMCs experience the combination of the local FUV radiation field flux (eq. 2) and the constant background field (eq. 3). The diffuse clouds are only exposed to the background field. In both GMCs and diffuse clouds, we adopt a spectral shape and luminosity corresponding to that of the local

Table 2. Adopted parameter values for the GMC grid and diffuse gas CLOUDY grids.

Parameter	Grid point values
GMCs:	
$\log(m_{\text{GMC}}/M_{\odot})$	[4.10, 4.28, 4.46, 4.64, 4.82, 5.00]
$\log(G_{0,\text{GMC}}/G_{0,\text{MW}})$	[0.80, 1.54, 2.28, 3.02, 3.76, 4.50]
$\log(Z/Z_{\odot})$	[-2.00, -1.64, -1.28, -0.92, -0.56, -0.20]
$\log(P_{\text{ext}}/\text{K cm}^{-3})$	[5.5, 6.4, 7.3, 8.2, 9.1, 10.0]
Diffuse gas:	
$\log(n_{\text{H}}/\text{cm}^{-3})$	[-3.50, -2.76, -2.02, -1.28, -0.54, 0.20]
$\log(R/\text{kpc})$	[-1.00, -0.76, -0.52, -0.28, -0.04, 0.20]
$\log(Z/Z_{\odot})$	[-3.00, -2.46, -1.92, -1.38, -0.84, -0.30]
$\log(T_{\text{k}}/\text{K})$	[2.50, 3.16, 3.82, 4.48, 5.14, 5.80]
$G_{0,\text{bg}}/G_{0,\text{MW}}$	[5, 35]

Solar neighborhood, which is then scaled by $G_{0,\text{GMC}}$ and $G_{0,\text{bg}}$ respectively.

Element abundances: In the MUFASA simulations, the abundances of He, C, N, O, Ne, Mg, Si, S, Ca and Fe (relative to H) are each tracked separately and self-consistently calculated at every time-step for each fluid element. While CLOUDY can take an abundance set as input parameter, it is unfeasible to run CLOUDY models for every distinct abundance pattern present in the MUFASA simulations. Our default approach is to ascribe the local ISM abundances to a cloud (dense or diffuse), but scale all element abundances by the metallicity inherited from the parent fluid element. Specifically, we scale the abundances from CLOUDY such that a sum over the mass fractions of the elements He, C, N, O, Ne, Mg, Si, S, Ca and Fe for a fluid element with solar metallicity gives 0.0134 as expected (Asplund et al. 2009).

Gas kinetic temperature: In the GMCs, CLOUDY is allowed to iterate for a temperature. For the diffuse clouds, we keep the temperature fixed at the grid parameter values listed in Table 2.

The dust content of each cloud is set to scale linearly with its metallicity, normalizing it to the grain abundance in the local ISM. The latter is stored in CLOUDY as graphite and silicate grain abundances divided into ten size bins, and corresponds to a dust-to-metal (DTM) ratio of 0.50 at solar metallicity. Further-

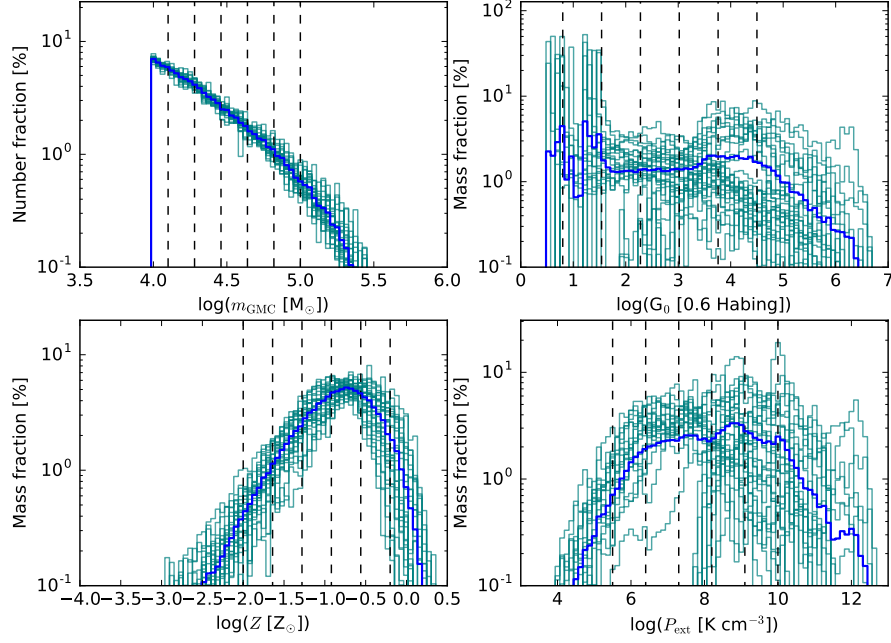


Figure 4. Histograms of m_{GMC} , $G_{0,\text{GMC}}$, Z , and P_{ext} of the GMCs in our 30 model galaxies (dark green histograms), with the mean histograms shown in blue. The vertical dashed lines indicate the chosen **CLOUDY** grid points (see §3.3).

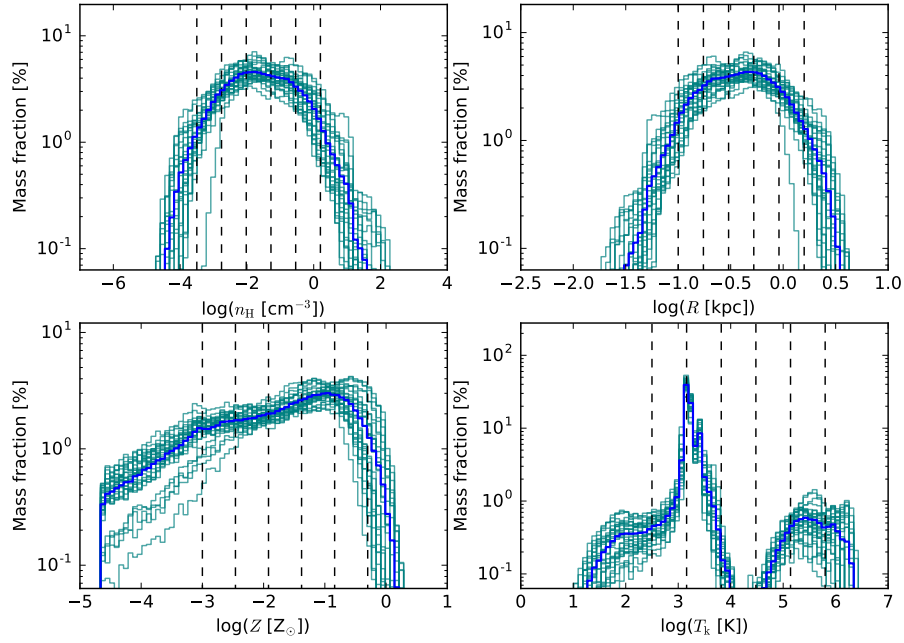


Figure 5. Histograms of n_{H} , R , Z , and T_{k} of the diffuse gas clouds in our 30 model galaxies (dark green histograms), with the mean histograms shown in blue. The vertical dashed lines indicate the chosen **CLOUDY** grid points (see §3.3).

more, dust sublimation is included in the diffuse gas models to allow for dust destruction in regions of high temperature. CLOUDY also allows for the inclusion of turbulence by specifying a microturbulent velocity. For the diffuse clouds we exclude turbulence by setting it to 0 km s^{-1} , after a test showed that setting the turbulence to 10 km s^{-1} only decreases the [C II] luminosities by on average 0.07 dex. For the GMCs we use the velocity dispersion obtainable from the cloud radius and pressure (see Olsen et al. 2015).

At $z \sim 6$ the CMB temperature is substantial ($\sim 19 \text{ K}$), and is included in the calculations of CLOUDY with the ‘CMB command’. The line intensities are corrected to give net line flux above the background continuum, including the diminution effect that happens when upper population levels are sustained by the CMB and reduce the rate of spontaneous de-excitations relative to when excitation happens by collisions only (see Ferland et al. 2017 for a more complete description of the CMB treatment in CLOUDY version 17).

CLOUDY divides each cloud into a number of shells when solving the radiative transfer, heat transfer and chemistry. We set the number of shells to ~ 50 , leading to a radial resolution in the range $\sim 0.01 - 0.52 \text{ pc}$ for the GMCs and $\sim 1 - 100 \text{ pc}$ for the diffuse gas clouds. Due to computational limitations that make it infeasible to run CLOUDY on every single cloud in our simulations, we construct grids of CLOUDY models, one grid for GMCs and another for the diffuse clouds, and interpolate over those. The GMC grid parameters consist of $[m_{\text{GMC}}, G_{0,\text{GMC}}, Z, P_{\text{ext}}]$ and the diffuse cloud parameters are $[n_{\text{H}}, R, Z, T_{\text{k}}]$. We ran diffuse gas model grids with $G_{0,\text{bg}}/G_{0,\text{MW}} = 5$, and 35 (eq. 3), which were the two values most of the galaxies clustered around. One galaxy (G21) has a diffuse FUV field of 120 times $G_{0,\text{MW}}$, but adding a further four diffuse gas model grids at $G_0/G_{0,\text{MW}} = 15, 25, 45$, and 120 to better sample the distribution did not significantly change the line emission properties of the simulations. The grid parameter values defining our grids are listed in Table 2, and indicated as vertical dashed lines in Figs. 4 and 5. Each grid consists of a total of 1296 CLOUDY models. The CLOUDY models were run on either the Stampede supercomputer at the Texas Advanced Computing Center⁷, the Saguaro cluster at ASU⁸ or the Pleiades supercomputer at NASA⁹.

4. SIMULATION RESULTS

4.1. The $L_{[\text{C II}]} - \text{SFR}$ relation at $z \simeq 6$

Fig. 6 (left panel) shows $L_{[\text{C II}]}$ against SFR for our model galaxies (filled circles). There seems to be a correlation between these two quantities, although our simulations only span about a decade in [C II] luminosity and SFR and there is significant scatter in $L_{[\text{C II}]}$, especially at the high-SFR end. A Pearson correlation coefficient test yields an R -value of 0.64 and a p -value of 0.00014 for the likelihood that the observed correlation could arise by chance if the quantities were uncorrelated. We can therefore meaningfully fit a log-linear relationship to the simulation points in Fig. 6. This yields:

$$\log(L_{[\text{C II}]} [L_{\odot}]) = (6.69 \pm 0.10) + (0.58 \pm 0.11) \times \log(\text{SFR} [\text{M}_{\odot} \text{ yr}^{-1}]), \quad (6)$$

which is shown as the purple dashed line in Fig. 6. The uncertainties on the slope and intercept were derived from bootstrapping the model results 5000 times. The r.m.s. scatter of the simulated galaxies around this relation is 0.15 dex (green shaded region).

Also shown in Fig. 6 are the more than two dozen $z \gtrsim 5$ galaxies observed in [C II] to date: 23 detections (filled symbols), and 14 non-detections (upper limits, open symbols). Only normal star forming galaxies (e.g., LBGs and LAEs) have been included in this tally (see Table 3) – possibly with the exception of a clump of gas that may not be star forming but was detected in [C II] in the vicinity of LBG BDF-3299 (Maiolino et al. 2015). Obvious AGN-dominated sources and QSOs have been omitted.

Based on these data, it would seem there is not a single $L_{[\text{C II}]} - \text{SFR}$ relation. There is a relation defined mainly by the $z \sim 5 - 6$ LBGs with $\text{SFR} \gtrsim 20 \text{ M}_{\odot} \text{ yr}^{-1}$ observed by Capak et al. (2015), Willott et al. (2015), Decarli et al. (2017) and Smit et al. (2017), which matches the locally observed $L_{[\text{C II}]} - \text{SFR}$ relation for starburst galaxies (De Looze et al. 2014) and is in agreement with simulations of main-sequence galaxies at $z \sim 2$ (Olsen et al. 2015) (see right-hand panel of Fig. 6). Offset from these points, there is a sequence of galaxies with significantly lower [C II] luminosities. These are predominantly LAEs with $\text{SFR} < 30 \text{ M}_{\odot} \text{ yr}^{-1}$, except for two notable high-SFR sources (Ouchi et al. 2013; Inoue et al. 2016). Since the majority of these sources have in fact only upper limit constraints on their [C II] luminosity (Kanevar et al. 2013; Ota et al. 2014; Maiolino et al. 2015; Knudsen et al. 2017) it is not clear whether or not they form a $L_{[\text{C II}]} - \text{SFR}$ relation of their own. However, the fact that our simulated galaxies coincide with these [C II]-

⁷ <https://www.tacc.utexas.edu/systems/stampede>

⁸ <https://researchcomputing.asu.edu/>

⁹ <https://www.nasa.gov/hecc/resources/pleiades.html>

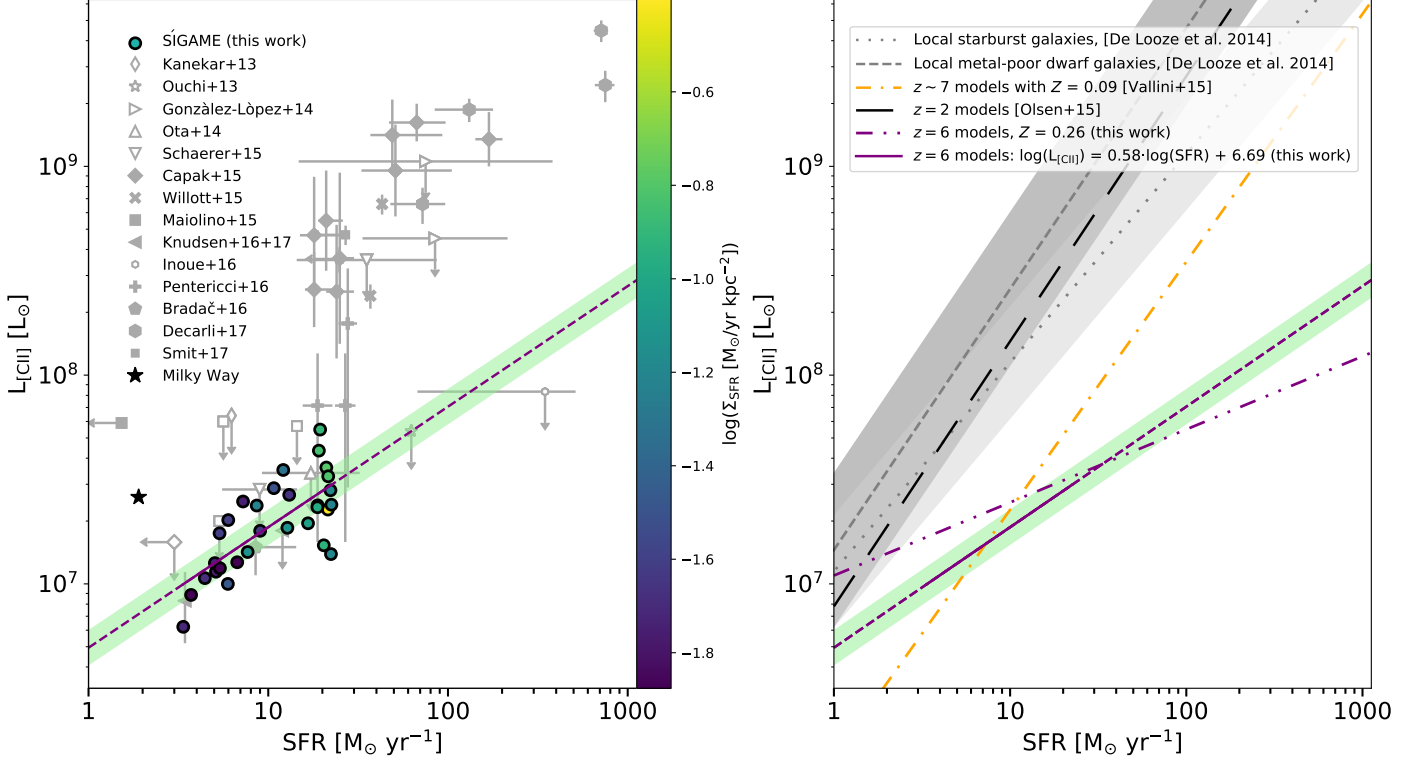


Figure 6. **Left:** the [C II] luminosity versus SFR for our simulations and the green shaded region delineates the scatter (0.13 dex) around this relation. For comparison all [C II] observations to date of LBGs and/or LAEs at $z \gtrsim 5$ are shown (grey symbols, where filled and open symbols indicate detections and $3\text{-}\sigma$ upper limits, respectively). For further details on the observations see Kanekar et al. (2013); Ouchi et al. (2013); González-López et al. (2014); Ota et al. (2014); Schaerer et al. (2015); Capak et al. (2015); Willott et al. (2015); Maiolino et al. (2015); Inoue et al. (2016); Pentericci et al. (2016); Knudsen et al. (2016, 2017); Bradač et al. (2017); Decarli et al. (2017); Smit et al. (2017). For the sake of clarity, we have not included MS0451-H ($z = 6.703$) in the plot. This source has $L_{[\text{C II}]} < 3 \times 10^5 L_{\odot}$ and $\text{SFR} \sim 0.4 M_{\odot} \text{ yr}^{-1}$ (Knudsen et al. 2017), and lies about 1 dex below our fitted relation. All SFRs have been converted to a Chabrier IMF where applicable. **Right:** a comparison with other, observed and simulated, [C II] – SFR relations. Shown are the [C II]–SFR relations derived by De Looze et al. (2014) for local metal-poor dwarf galaxies (grey dashed line) and local starburst galaxies (grey dotted line); grey dashed and dotted lines, respectively, with the shaded regions indicating the r.m.s. scatter of these relations). Also shown are simulated relations of $z = 2$ main sequence galaxies (black long dashed line; Olsen et al. (2015)) and $z \sim 7$ galaxies (orange dash-dotted line; Vallini et al. (2015)).

faint sources in the panel suggests that our models are representative of the observations. Furthermore, eq. 6 is consistent with the two high-SFR, [C II] upper limits by Ouchi et al. (2013) and Inoue et al. (2016). On the other hand, MS0451-H ($z = 6.703$; Knudsen et al. 2017) with its extremely low [C II] luminosity ($< 3 \times 10^5 L_{\odot}$) and SFR ($\sim 0.4 M_{\odot} \text{ yr}^{-1}$) falls below eq. 6 by about 1 dex (not shown due to the axis range of the Fig. 6). Clearly, more sensitive observations, and of a larger sample of galaxies, are required to delineate a [C II] – SFR relation at this epoch.

In Fig. 6 (right panel) we compare our eq. 6 with the $z \simeq 7$ [C II]–SFR relation by Vallini et al. (2015). The latter is derived from a fiducial simulation of a single $z \sim 7$ galaxy, and scaling its $L_{[\text{C II}]}$ and SFR according to $L_{[\text{C II}]} \propto M_{\text{H}_2}$ and $\Sigma_{\text{SFR}} \propto \Sigma_{\text{H}_2}$. Also, the gas phase metallicity of the galaxy is fixed to a constant

value throughout the galaxy and bears therefore no relation to its star formation history. By adopting a set of fixed metallicities, Vallini et al. (2015) arrives at an expression for $L_{[\text{C II}]}$ as a function of SFR and metallicity. The orange dash-dotted line in the right-hand side panel shows their [C II]–SFR relation for a uniform metallicity equal to the mean mass-weighted metallicity of our simulated galaxies ($0.09 \times Z_{\odot}$). This relation matches our simulated galaxies surprisingly well given the significant differences between their simulations and ours (see §5). Clearly, at SFR values outside the range of our simulations there is significant discrepancy between the [C II]–SFR relation by Vallini et al. (2015) and ours (eq. 6), owing to the much shallower slope of the latter (0.58 ± 0.11 versus 1.2). Extrapolating eq. 4 to SFRs well outside the range of the simulations is obviously fraught with danger and any comparison must be made

Table 3. All [C II] observations in the literature to date of $z \gtrsim 5$ star forming galaxies. Obvious AGN-dominated sources and QSOs have not been included. Star formation rates and [C II] luminosities have been corrected for gravitational magnification (μ). Upper limits are $3\text{-}\sigma$ limits.

Name	z	SFR ^a [$M_{\odot} \text{ yr}^{-1}$]	$L_{[\text{C II}]}$ [L_{\odot}]	μ^b	Reference
HZ8	5.1533	18 ^e	2.57×10^9	...	Capak et al. (2015)
HZ7	5.2532	21 ^e	5.50×10^9	...	Capak et al. (2015)
HZ6	5.2928	49 ^e	1.41×10^{10}	...	Capak et al. (2015)
HZ5	5.3089	$< 3^e$	$< 1.58 \times 10^7$...	Capak et al. (2015)
HZ9	5.5410	67 ^e	1.62×10^{10}	...	Capak et al. (2015)
HZ3	5.5416	18 ^d	4.68×10^8	...	Capak et al. (2015)
HZ4	5.5440	51 ^e	9.55×10^8	...	Capak et al. (2015)
HZ10	5.6566	169 ^e	1.34×10^{10}	...	Capak et al. (2015)
HZ2	5.6697	25 ^e	3.63×10^8	...	Capak et al. (2015)
HZ1	5.6885	24 ^e	2.51×10^8	...	Capak et al. (2015)
A383-5.1	6.0274	$3.2\text{--}3.7^d$	$< 8.3 \times 10^6$	11.4 ± 1.9	Knudsen et al. (2016)
SDSS J0842+1218 comp	6.0656	131 ^f	1.87×10^9	...	Decarli et al. (2017)
WMH5	6.0695	43 ^c	6.6×10^8	1.27	Willott et al. (2015)
CFHQ J2100-1715 comp	6.0796	750 ^f	2.45×10^9	...	Decarli et al. (2017)
CLM1	6.1657	37 ^c	2.4×10^8	...	Willott et al. (2015)
PSO J308-21 comp	6.2485	72 ^f	6.6×10^8	...	Decarli et al. (2017)
SDF J132415.7	6.541	$34\text{--}211.2^d$	$< 4.52 \times 10^8$	< 1.1	González-López et al. (2014)
SDF J132408.3	6.554	$15\text{--}375.9^d$	$< 10.56 \times 10^8$	< 1.1	González-López et al. (2014)
HCM 6A	6.56	6.25 ^c	$< 0.64 \times 10^8$	≈ 4.5	Kanekar et al. (2013)
PSO J231-20 comp	6.5900	713 ^f	4.47×10^9	...	Decarli et al. (2017)
Himiko	6.595	62.5 ^c	$< 0.54 \times 10^8$...	Ouchi et al. (2013)
UDS16291	6.6381	$15.8\text{--}22.4^d$	7.15×10^7	...	Pentericci et al. (2016)
NTTDF6345	6.701	$25\text{--}30.7^d$	1.77×10^8	...	Pentericci et al. (2016)
MS0451-H	6.703	$0.4\text{--}0.47^d$	$< 3 \times 10^5$	100 ± 20	Knudsen et al. (2016)
RXJ1347:1216	6.7655	8.5 ^c	1.5×10^7	5 ± 0.3	Bradač et al. (2017)
A1703-zD1	6.8	$5.6\text{--}14.3^d$	$< 2.83 \times 10^7$	~ 9	Schaerer et al. (2015)
COS-2987030247	6.8076	$16\text{--}38.7^d$	3.6×10^8	...	Smit et al. (2017)
SDF-46975	6.844	14.4 ^e	$< 5.7 \times 10^7$...	Maiolino et al. (2015)
COS-3018555981	6.8540	$19\text{--}38.2^d$	4.7×10^8	...	Smit et al. (2017)
IOK-1	6.96	$9.4\text{--}31.8^d$	$< 3.4 \times 10^7$...	Ota et al. (2014)
BDF-512	7.008	5.6 ^e	$< 6 \times 10^7$...	Maiolino et al. (2015)
BDF-3299 (clump A)	7.107	$< 1.5^e$	5.9×10^7	...	Maiolino et al. (2015)
BDF-3299	7.109	5.3 ^e	$< 2 \times 10^7$...	Maiolino et al. (2015)
COSMOS13679	7.1453	$23.9\text{--}30^d$	7.12×10^7	...	Pentericci et al. (2016)
SXDF-NB1006-2	7.2120	347 ^c	$< 8.4 \times 10^7$...	Inoue et al. (2016)
z8-GND-5296	7.508	$14.6\text{--}85.3^d$	$< 3.56 \times 10^8$	~ 9	Schaerer et al. (2015)
A1689-zD1	7.6031	12 ^e	1.8×10^7	9.5	Knudsen et al. (2017)

^a SFRs are for a Chabrier IMF. SFRs based on a Kroupa or Salpeter IMF were corrected by a factor 1.5/1.6 and 1/1.6, respectively.

^b Where the magnification factor is unknown, we assume a value of 1.

^c SED-based SFR.

^d Low SFRs are derived from the UV; high SFRs are from the UV combined with an upper limit in the IR.

^e UV-based SFR.

^f IR-based SFR.

with caution. This is especially true given that eq. 4 is a fit to a set of simulations which span no more than a decade in SFR and $L_{[\text{C II}]}$.

4.2. ISM phases and $[\text{C II}]$

The mass fractions of each ISM phase stay relatively constant across the 30 simulated galaxies: the GMCs, diffuse neutral and diffuse ionized gas take up on average $\sim 10\%$, $\sim 6\%$ and $\sim 85\%$ of the total ISM mass, respectively, and there is no apparant trend with SFR or $\langle Z \rangle_{\text{mass}}$ (Fig. 7, top panels). In contrast, the contribution of these ISM phases to the total $[\text{C II}]$ luminosity can vary significantly from one simulated galaxy to another. The GMCs take up $\sim 5 - 63\%$ (average $\sim 27\%$), the diffuse neutral gas $\sim 1 - 23\%$ (average $\sim 7\%$), and the diffuse ionized gas $\sim 36 - 90\%$ (average $\sim 66\%$) of the total $[\text{C II}]$ luminosity. The dominant source of $[\text{C II}]$ in the simulated galaxies is either the diffuse ionized gas or the GMCs, with the diffuse neutral gas making up a minor contribution ($\lesssim 23\%$).

In Fig. 7 (middle panels) the ISM phase contributions to $L_{[\text{C II}]}$ are shown as a function of galaxy SFR (left panel) and $\langle Z \rangle_{\text{mass}}$ (right panel). The contribution from the diffuse ionized gas, which is the dominant phase in nearly all the galaxies, tends to increase slightly towards the high-end of the SFR and $\langle Z \rangle_{\text{mass}}$ distributions. For the GMCs and the diffuse neutral gas the tendency is in the opposite direction, i.e., their contributions tend to increase toward lower SFR and $\langle Z \rangle_{\text{mass}}$.

In the Vallini et al. (2015) models with SFRs similar to our simulations, $\lesssim 10\%$ of the total $[\text{C II}]$ emission is coming from diffuse neutral gas, with the remainder coming from PDRs associated with molecular gas. Thus, to the extent that the diffuse neutral gas in the two simulations map onto each other, there is broad agreement about the contribution of this phase to the total $[\text{C II}]$ luminosity. The lower $[\text{C II}]$ contributions from molecular gas in our simulations compared to the Vallini et al. (2015) models ($\sim 37\%$ vs. $\gtrsim 90\%$) must, in part at least, be due to the fact that Vallini et al. (2015) do not include a hot diffuse ionized phase. In contrast, the diffuse ionized gas mass fraction in our simulations is $\sim 85\%$ on average and is responsible for more than half of the total $[\text{C II}]$ luminosity in most of our simulations. In our Milky Way, dense PDRs and CO-dark H_2 gas is responsible for about $\sim 55\%$ of the total $[\text{C II}]$ emission, while the diffuse ionized gas and diffuse neutral gas contribute $\sim 20\%$ and 25% , respectively (Pineda et al. 2014). Cormier et al. (2012) used CLOUDY to model the ISM of the nearby ($z \sim 0.021$) starburst galaxy Haro 11, which has a metallicity ($\sim 0.3 Z_\odot$) and a SFR ($\sim 22 \text{ M}_\odot \text{ yr}^{-1}$) matching that of our simulations, and found that 10% of the $[\text{C II}]$

luminosity comes from dense PDRs and about 50% from the diffuse ionized medium.

We have seen that the galaxy-to-galaxy variations in the relative $[\text{C II}]$ contributions from the ISM phases are not matched by their (nearly constant) mass fractions. This suggests that the ability of a given ISM phase to shine in $[\text{C II}]$ can change significantly among different galaxies. In order to investigate this, we plot in Fig. 7 (bottom panels) the $[\text{C II}]$ efficiency, defined as $[\text{C II}]$ luminosity over gas mass, in order of increasing SFR (left panel) and $\langle Z \rangle_{\text{mass}}$ (right panel).

Although there are notable exceptions, the $[\text{C II}]$ efficiencies of all three phases tend to increase with SFR and with $\langle Z \rangle_{\text{mass}}$. The trend with metallicity is easily understood, as an increase in the carbon abundance will result in a higher abundance of C^+ . The trend with SFR is a combination of the fact that our simulations with higher SFR have higher metallicities (see Table 1) and the fact that, on average, they have stronger FUV radiation fields capable of ionising a larger fraction of the neutral carbon in the GMC and diffuse neutral phase.

4.3. $[\text{OI}]$ and $[\text{O III}]$ at $z \simeq 6$

In this section we shall examine the $[\text{OI}]$ $63 \mu\text{m}$ and $[\text{O III}]$ $88 \mu\text{m}$ line emission from our simulations. Fig. 8 shows $[\text{OI}]$ and $[\text{O III}]$ luminosities vs. SFRs for our simulated galaxies, along with local $L_{[\text{OI}]} - \text{SFR}$ and $L_{[\text{O III}]} - \text{SFR}$ relations established for samples of local metal-poor dwarfs and starburst galaxies (De Looze et al. 2014). Both the $[\text{OI}]$ and $[\text{O III}]$ simulations overlap with the local relations, although the agreement is significantly better for $[\text{O III}]$ than for $[\text{OI}]$. In fact, the $[\text{OI}]$ simulations exhibit no correlation with SFR: a Pearson correlation test of $\log(L_{[\text{OI}]})$ vs. $\log(\text{SFR})$ gives R - and p -values of -0.08 and 0.69 , respectively. In contrast, $[\text{O III}]$ shows a strong correlation with SFR, and a Pearson correlation test of $\log(L_{[\text{O III}]})$ vs. $\log(\text{SFR})$ yields $R = 0.79$ and $p = 2.5 \times 10^{-7}$, respectively. Thus, the $[\text{O III}]$ luminosities of our simulations correlate more strongly with SFR than $[\text{C II}]$. A log-linear fit yields:

$$\log(L_{[\text{O III}]} [L_\odot]) = (6.27 \pm 0.14) + (1.12 \pm 0.17) \times \log(\text{SFR} [\text{M}_\odot \text{ yr}^{-1}]), \quad (7)$$

which is shown as the purple dashed line in Fig. 8. The uncertainties on the slope and intercept were inferred from bootstrapping in a similar way as for $[\text{C II}]$ (§4.1). The $[\text{O III}]$ detection by Laporte et al. (2017) of a $z = 8.38$ star forming galaxy ($\text{SFR} \simeq 20 \text{ M}_\odot \text{ yr}^{-1}$) matches extremely well our simulations with similar SFRs. Furthermore, extrapolating eq. 7 to the SFR

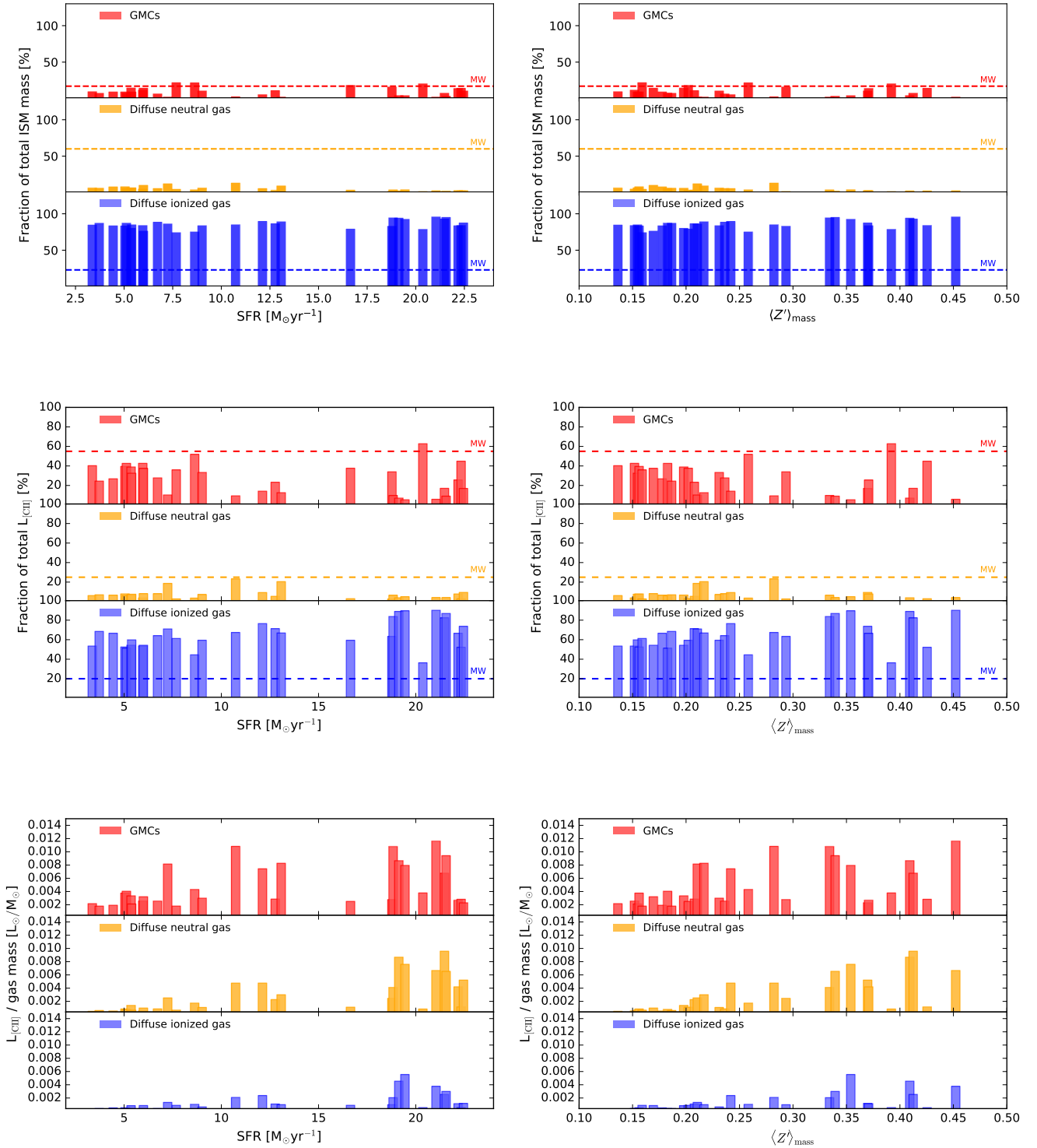


Figure 7. Top: Mass fractions of the three ISM phases of our simulated galaxies as a function of their total SFRs (left panel) and mass-weighted average metallicities, $\langle Z \rangle_{\text{mass}}$ (right panel). The three ISM phases, GMCs, diffuse neutral gas and diffuse ionized gas, are shown as red, orange and blue shaded regions, respectively. The corresponding mass fractions in the MW have been shown with horizontal dashed lines: 17% H_2 (red), 60% H I (orange) and 23% H II (blue) within 20kpc with numbers from [Draine \(2011\)](#). **Middle:** The contributions from the ISM phases to the total [C II] luminosities vs. SFRs (left panel) and $\langle Z \rangle_{\text{mass}}$ (right panel). The horizontal dashed lines indicate the corresponding fractions for the MW ([Pineda et al. 2014](#)). **Bottom:** The [C II] luminosity per gas mass of each ISM phase vs. SFRs (left panel) and $\langle Z \rangle_{\text{mass}}$ (right panel).

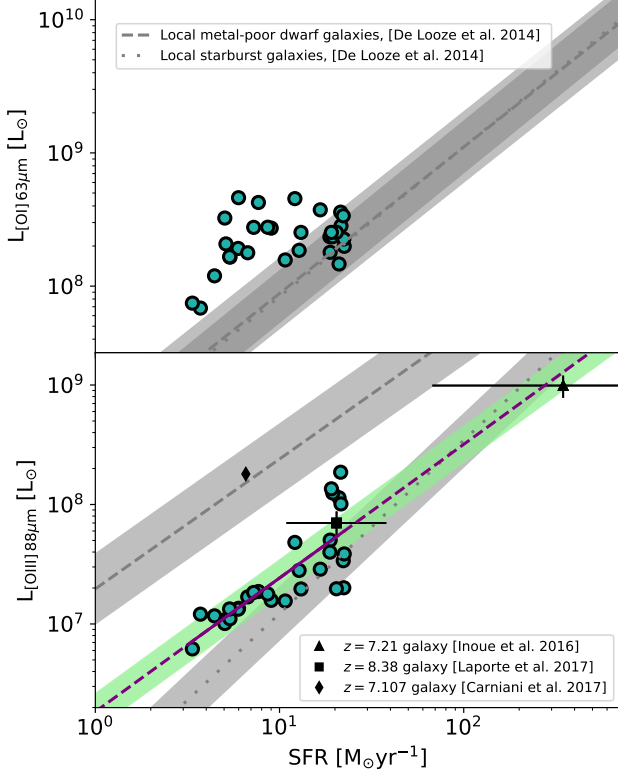


Figure 8. $L_{[\text{OI}]}$ vs. SFR (top) and $L_{[\text{OIII}]}$ vs. SFR (bottom) for our simulated galaxies (filled circles) compared to $z \gtrsim 5$ observations of the two lines. A log-linear fit to the [O III] simulations is shown by the purple dashed line with a 1σ scatter (0.15 dex) in $L_{[\text{OIII}]}$ as indicated by the green shaded region. Local relations for metal-poor dwarf galaxies (grey dashed lines) and local starburst galaxies (grey dotted lines) are shown for comparison (De Looze et al. 2014). The grey-shaded regions indicate the $\pm 1\sigma$ scatter around these relations. Also shown are the detections to date of [O III] in star forming galaxies at $z \gtrsim 5$ (Inoue et al. 2016; Laporte et al. 2017; Carniani et al. 2017).

($\sim 250 M_{\odot} \text{ yr}^{-1}$) of the detected LAE at $z = 7.21$ (Inoue et al. 2016) also results in an excellent match. Carniani et al. (2017) also reported three ‘blind’ [O III] detections in the vicinity of BDF-3299 (and at the same redshift). In Fig. 8, we only show the [O III] detection spatially closest to the clump detected in [C II] emission (Maiolino et al. 2015). Based on a comparison between models and this [O III] detection, Carniani et al. (2017) find that an in-situ SFR of $\sim 7 M_{\odot} \text{ yr}^{-1}$ is required ($\sim 6.6 M_{\odot} \text{ yr}^{-1}$ when converted from a Kroupa to a Chabrier IMF), bringing this object into agreement with the local metal-poor galaxies, but still about 1 dex above our models. The [O III] luminosities of the remain-

ing two sources are 2.2 and $5.8 \times 10^8 L_{\odot}$ (Carniani et al. 2017).

4.4. [C II] luminosity and global galaxy properties

In addition to SFR there are likely a number of other galaxy properties affecting the [C II] emission. For example, in §4.2 we found that the relative ISM phase contributions to the total [C II] luminosity of our simulated galaxies varied not only with SFR but also with average mass-weighted metallicity of the galaxies. This would suggest that the metallicity might have an effect on the $L_{[\text{C II}]} - \text{SFR}$ relation. The simulations by Vallini et al. (2015) exhibited an increase in the [C II] emission with metallicity, which at a basic level is expected since the [C II] cooling function scales linearly with the gas phase metallicity (Röllig et al. 2006). Observations of nearby galaxies have also found that surface density of SFR, Σ_{SFR} , can be important for the total amount of [C II] emitted. For example, Smith et al. (2017) found that the ratio of [C II]-to-IR luminosity decreases with increasing Σ_{SFR} across six orders of magnitude in Σ_{SFR} . Finally, we might expect that the more massive the gas reservoir of a galaxy, the more single ionised carbon is available and, therefore, the brighter the galaxy will shine in [C II].

In Fig. 9 we have plotted $L_{[\text{C II}]}$ of our simulated galaxies against their $\langle Z \rangle_{\text{SFR}}$, Σ_{SFR} and M_{ISM} (these quantities are given in Table 1, and $M_{\text{ISM}} = M_{\text{gas}}$). $L_{[\text{C II}]}$ appears to correlate with $\langle Z \rangle_{\text{SFR}}$ and Σ_{SFR} , whereas there seems to be no discernable correlation with M_{ISM} – perhaps due to the small range spanned in gas mass by our simulations.

In order to better examine the dependence of $L_{[\text{C II}]}$ on the above quantities, and to account for their inter-dependance, we perform a principle component analysis (PCA; Jolliffe 2002) analysis. Normalizing the logarithm of the aforementioned quantities (and SFR) to zero mean leaves the following variables for the PCA:

$$\begin{aligned} x_1 &= \log(\text{SFR}) - 1.02 \\ x_2 &= \log(\langle Z \rangle_{\text{SFR}}) - (-0.61) \\ x_3 &= \log(\Sigma_{\text{SFR}}) - (-1.33) \\ x_4 &= \log(M_{\text{ISM}}) - 10.04 \end{aligned} \quad (8)$$

The resulting principle components in this four dimensional parameter space are:

$$\begin{aligned} \text{PC}_1 &= 0.52x_1 + 0.28x_2 + 0.80x_3 - 0.10x_4 \\ \text{PC}_2 &= 0.64x_1 + 0.36x_2 - 0.48x_3 + 0.47x_4 \\ \text{PC}_3 &= 0.53x_1 - 0.45x_2 - 0.27x_3 - 0.66x_4 \\ \text{PC}_4 &= 0.18x_1 - 0.76x_2 + 0.22x_3 + 0.57x_4. \end{aligned} \quad (9)$$

88% of the sample variance is contained within the eigenvector PC_1 which is dominated by and increases

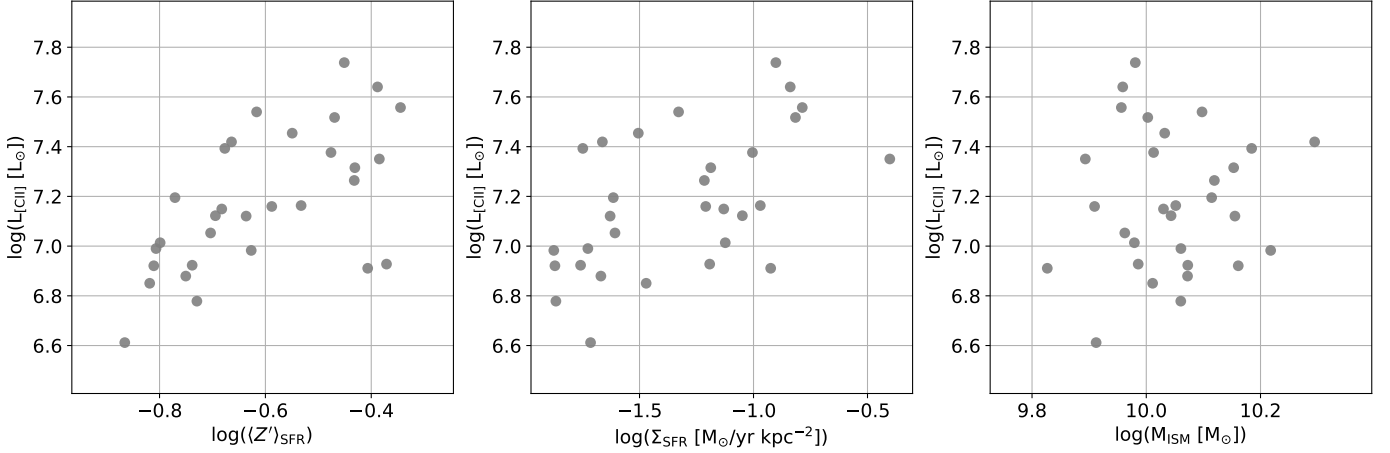


Figure 9. L_{CII} versus $\langle Z \rangle_{\text{SFR}}$ (left), Σ_{SFR} (middle) and M_{ISM} (right) for simulated galaxies.

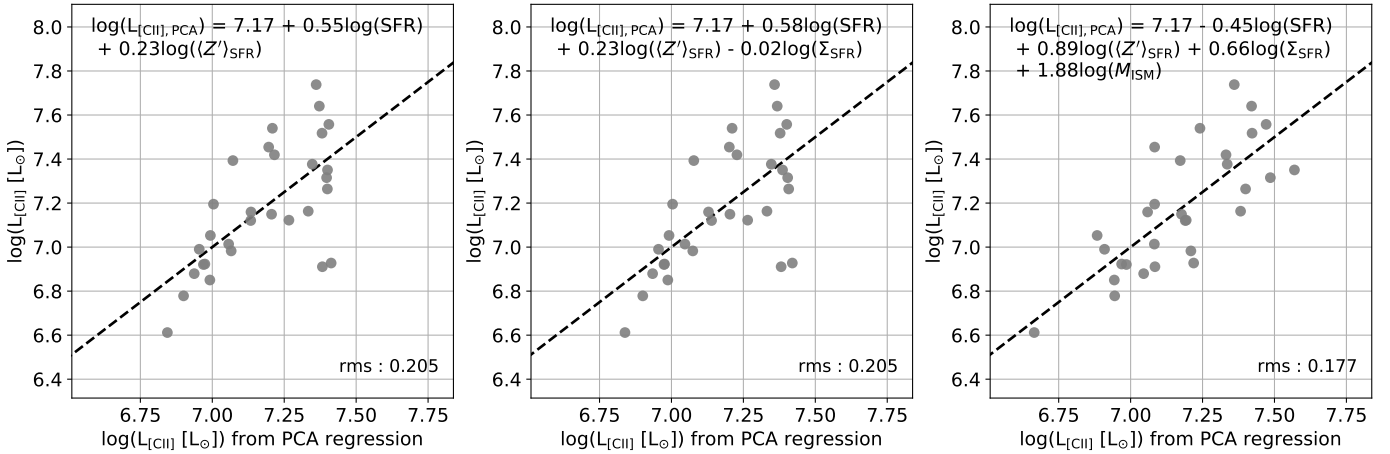


Figure 10. Results of a PCA regression to the [C II] luminosities of our simulations using different sets of free parameters. **Left panel:** SFR and $\langle Z \rangle_{\text{SFR}}$ (see eq. 13). **Middle panel:** SFR, $\langle Z \rangle_{\text{SFR}}$ and Σ_{SFR} (see eq. 12). **Right panel:** SFR, $\langle Z \rangle_{\text{SFR}}$, Σ_{SFR} and M_{ISM} (see eq. 11). The dashed lines indicate the 1:1 line. The r.m.s. scatter of the simulations with respect to eqs. 11, 12, and 13 are indicated.

strongly with SFR and Σ_{SFR} . PC_2 , PC_3 and PC_4 contain ~ 9 , 0.6 and 2.3% of the variance, respectively. Thus of the global galaxy properties considered, the star formation activity is the most important factor for driving the [C II] luminosity.

Keeping all four principle components, a regression can be made to:

$$\log(L_{\text{CII}}) = \beta_0 + \beta_1 \text{PC}_1 + \beta_2 \text{PC}_2 + \beta_3 \text{PC}_3 + \beta_4 \text{PC}_4, \quad (10)$$

leading to the following relation for L_{CII} :

$$\log(L_{\text{CII}}) = 7.17 - 0.45 \log(\text{SFR}) + 0.89 \log(\langle Z \rangle_{\text{SFR}}) + 0.66 \log(\Sigma_{\text{SFR}}) + 1.88 \log(M_{\text{ISM}}). \quad (11)$$

In Fig. 10 (right hand panel) we show the [C II] luminosities obtained by applying eq. 11 to our model galaxies plotted against their true [C II] luminosities from the simulations. The scatter between the true [C II] luminosities of the galaxies and eq. 11 is only 0.18 dex, suggesting that eq. 11 captures most of the [C II] dependencies on global galaxy parameters. Repeating the above PCA and regression analysis but using only (SFR, $\langle Z \rangle_{\text{SFR}}$, Σ_{SFR}) and (SFR, $\langle Z \rangle_{\text{SFR}}$) as free parameter sets, we obtain:

$$\log(L_{\text{CII}}) = 7.17 - 0.58 \log(\text{SFR}) + 0.23 \log(\langle Z \rangle_{\text{SFR}}) - 0.02 \log(\Sigma_{\text{SFR}}), \quad (12)$$

and

$$\log(L_{\text{CII}}) = 7.17 + 0.55 \log(\text{SFR}) + 0.23 \log(\langle Z \rangle_{\text{SFR}}),$$

(13)

respectively. It is seen that limiting the free parameters to $(\text{SFR}, \langle Z \rangle_{\text{SFR}}, \Sigma_{\text{SFR}})$ (middle panel) or $(\text{SFR}, \langle Z \rangle_{\text{SFR}})$ (left panel), deteriorates the correlations somewhat, with a slight increase in the scatter as a result (0.21 dex).

5. DISCUSSION

5.1. Simulation robustness

In this section we examine the effects on the simulation outcomes when changing some of the assumptions build into SÍGAME (§3). To this end, we ran SÍGAME on the same 30 MUFASA simulations presented in §2 but with changes made to: 1) the dust-to-metals mass ratio, 2) the slope of the GMC mass spectrum, or 3) the element abundances.

The dust-to-metals mass ratio. The simulations presented in this paper have adopted a DTM mass ratio of 0.5, close to ~ 0.62 of the MW (the latter derived from an average over 243 lines of sight through the local part of our Galaxy; Wiseman et al. 2017). However, recent studies at high redshifts have shown that dust production is less efficient at low metallicities resulting in DTM mass ratios significantly below that of the MW in low metallicity systems (Vladilo 2004; De Cia et al. 2013, 2016; Wiseman et al. 2017).

We ran SÍGAME using new grids of CLOUDY models with a DTM ratio of 0.25, i.e., half of that adopted in §3.3. The effect is to increase the [C II] luminosities of the simulated galaxies by $\sim 43\%$ on average or 0.15 dex and the change to the $L_{[\text{C II}]}-\text{SFR}$ relation is therefore significant (Fig. 11, left panel). The increase in $L_{[\text{C II}]}$ is primarily coming from the GMCs, where decreasing the amount of dust reduces the shielding of the gas from FUV radiation, thereby allowing for larger C^+ envelopes.

The GMC mass distribution. In high- z environments the GMCs are likely to differ from the Galactic mass spectrum (slope $\beta = 1.8$), which was adopted for our simulations (§3.1). In our Local Group alone, where GMC masses can be measured, significant variations in β have been found: from $\beta = 1.5$ in the inner MW to $\beta = 2.1$ and $\beta = 2.9$ in the outer MW and in M33, respectively (Rosolowsky 2005; Blitz et al. 2007). Running SÍGAME with a ‘bottom-heavy’ ($\beta = 3.0$) GMC mass spectrum has practically no impact on the [C II] emission of the galaxies, but switching to a ‘top-heavy’ ($\beta = 1.5$) GMC mass spectrum increases $L_{[\text{C II}]}$ by an average of 44 % or 0.15 dex (Fig. 11, middle panel), similar to the case of reduced DTM ratio.

Abundances. As we saw in §3.3 SÍGAME ascribes to a cloud (dense or diffuse) the element abundances of the local ISM, but scaled by the metallicity of the parent fluid element. This ensures a one-to-one relation between the abundance of an element and the metallicity, which is required in order to keep the number of CLOUDY models at a manageable level. These relations (one for each element) can easily be converted to relations between element mass fractions and metallicity and are plotted (green dash-dotted lines) in Fig. 12, which shows element mass fractions against metallicity for the fluid elements in three of the MUFASA galaxy simulations. It is seen that this approach does not match the element mass fractions of the simulations particularly well.

As a result, an alternative approach was devised, that would ensure that the element abundances provided as input to CLOUDY did in fact reflect the typical element mass fractions in the MUFASA simulations. In this approach a one-to-one relation between the mass fraction of an element and the metallicity is established by simply doing spline-fits to the average mass fractions within 100 bins in metallicity (purple dashed curve in Fig. 12). It is then straightforward to infer the corresponding element abundances (as a function of metallicity). Adopting this approach tends to lower the [C II] luminosities of our simulations, although in some cases there is actually a very slight increase. The net outcome is a shallower $L_{[\text{C II}]}-\text{SFR}$ relation (Fig. 11, right panel), but one which remains consistent with the [C II]-faint observations. The lower [C II] luminosities are due to the fact that over the metallicity range spanning the majority of both dense and diffuse clouds in the simulations ($-1.5 \lesssim \log Z/Z_{\odot} \lesssim 0$; Fig. 4 and 5), the default local ISM abundances (green dash-dotted lines) overshoot the average simulation carbon abundances (purple dashed curves).

5.2. Reconciling [CII]-luminous sources at $z \sim 6$ with our simulations

In the previous section we saw that our simulation findings are relatively robust against changes in some of the model assumptions. In particular, we saw that it is difficult to increase the [C II] emission from the simulations. This then begs the question of how to account for the [C II]-luminous LBGs detected by Capak et al. (2015), Willott et al. (2015) and Smit et al. (2017) (and the luminous QSO companions detected by Decarli et al. 2017), which lie significantly above the $L_{[\text{C II}]}-\text{SFR}$ relation defined by our simulations and the many [C II]-faint sources (e.g., Maiolino et al. 2015; Bradač et al. 2017).

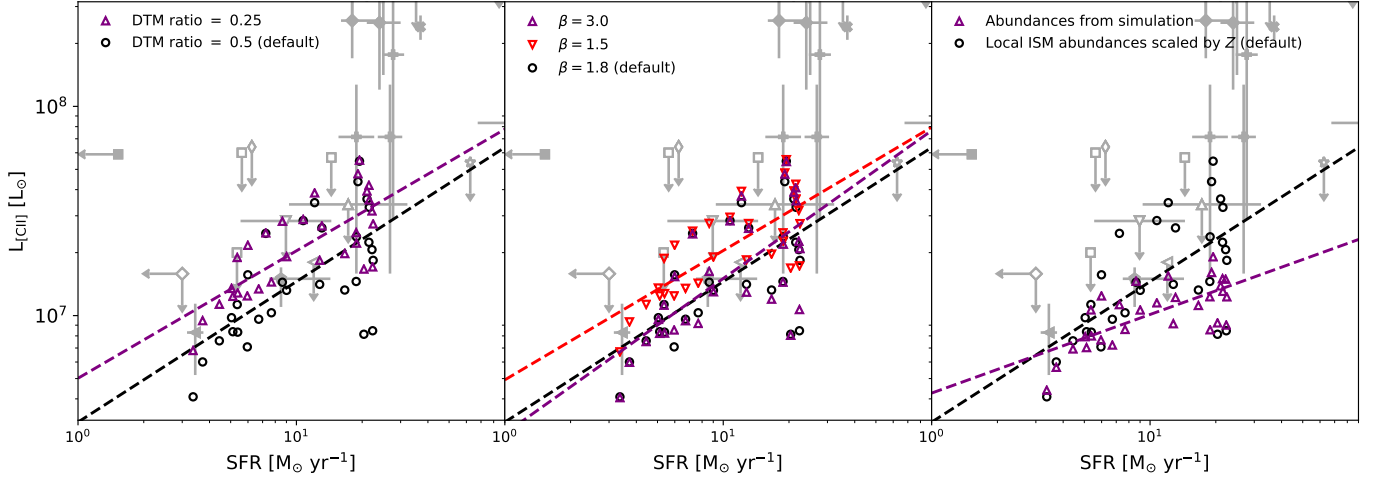


Figure 11. The result of deviating from the default assumptions of **SfGAME**. Purple triangles show the simulated galaxies in the $L_{[\text{CII}]}$ -SFR diagram after: reducing the DTM ratio by a factor 2 (left); changing the GMC mass spectrum to one that is more bottom- or top-heavy (middle); adopting abundances that better match the cosmological simulation (right). Black circles show the location of model galaxies with the default assumptions of **SfGAME**. Observations are shown with grey symbols as in Fig. 6.

Observational uncertainties. The SFRs of galaxies at $z \sim 6$ are derived via either conversion from IR luminosities or rest-frame UV continuum luminosities (corrected for dust). Although there can be significant uncertainties associated with estimating SFRs of high- z galaxies, in the case of the Capak et al. (2015) and Willott et al. (2015) LBGs they would have had to be underestimated by an order of magnitude if this was the reason for the above discrepancy. Capak et al. (2015) estimates a systematic uncertainty of 0.3 dex on the IR luminosities, which are inferred from only a single long-wavelength ($\lambda_{\text{obs}} = 0.85 - 1 \text{ mm}$) data-point and scaling a modified black body laws to it with dust temperatures in the range 25 – 45 K, spectral indices of 1.2 – 2.0, and Wien power-law slopes of 1.5 – 2.5.

We have made an estimate of the dust temperatures in our model galaxies using the dust radiative transfer package **powderday** (Narayanan et al. 2015, 2017) to generate dust emission SEDs for the central halos that we extract galaxies from. **powderday** builds off of **HYPERION** (Robitaille 2011; Robitaille et al. 2012), **FSPS** (Conroy et al. 2009, 2010), and **YT** (Turk et al. 2011). In short, **powderday** generates stellar spectra for all the stars formed in the simulation using their ages and metallicities, and computing their SEDs as simple stellar populations using **FSPS**. The metal properties of the model galaxies are projected onto an adaptive grid with an octree memory structure using **YT**, and then the stellar SEDs are propagated through the dusty ISM using **HYPERION** as the dust radiative transfer solver. This process is iterated upon in a Monte Carlo fashion until the radiation field and dust temperatures

have achieved equilibrium. Since we only extract central galaxies, these SEDs will be dominated by the light from our simulated galaxies. The resulting dust temperatures lie in the range 50 – 72 K, i.e., significantly warmer than the Capak et al. (2015) sources. If $> 50 \text{ K}$ is a more appropriate temperature range for the dust in $z \sim 6$ LBGs, it would imply that their IR luminosities had been underestimated. Whether this also implies higher star formation rates is less clear. We note that this is a good bit warmer than the typical dust temperature of simulations of comparable luminosity galaxies at $z \sim 0 - 2$ (e.g. Narayanan et al. 2010, 2011); this is due principally to the low dust contents and hard radiation fields in low-metallicity galaxies at $z > 5$.

AGN. The possibility that the $[\text{CII}]$ -brightness of the Capak et al. (2015) and Willott et al. (2013) sources could be due to the presence of AGN seems unlikely since normal LBGs at $z \sim 6$ are expected to have moderate mass black holes ($\lesssim 10^8 M_{\odot}$) that would not dominate the overall energetics. Also, $[\text{CII}]$ observations of QSOs at $z \sim 6$ (and at lower redshifts) tend to show lower, not higher, $L_{[\text{CII}]} / L_{\text{IR}}$ values compared to star forming galaxies (Maiolino et al. 2005; Venemans et al. 2012; Wang et al. 2013a; Zhao et al. 2016).

Gas mass fractions. Is it possible that our simulations and the $[\text{CII}]$ -faint sources have significantly lower gas mass fractions, and thus smaller gas reservoirs that can emit in $[\text{CII}]$, than the $[\text{CII}]$ -bright LBGs? In §4.2 we found that the molecular and diffuse ionized gas phases contribute about equally to the total $[\text{CII}]$ luminosities of simulations with $\text{SFR} \lesssim 10 M_{\odot} \text{ yr}^{-1}$, while at higher SFRs the ionized gas tends to dominate. Taking these

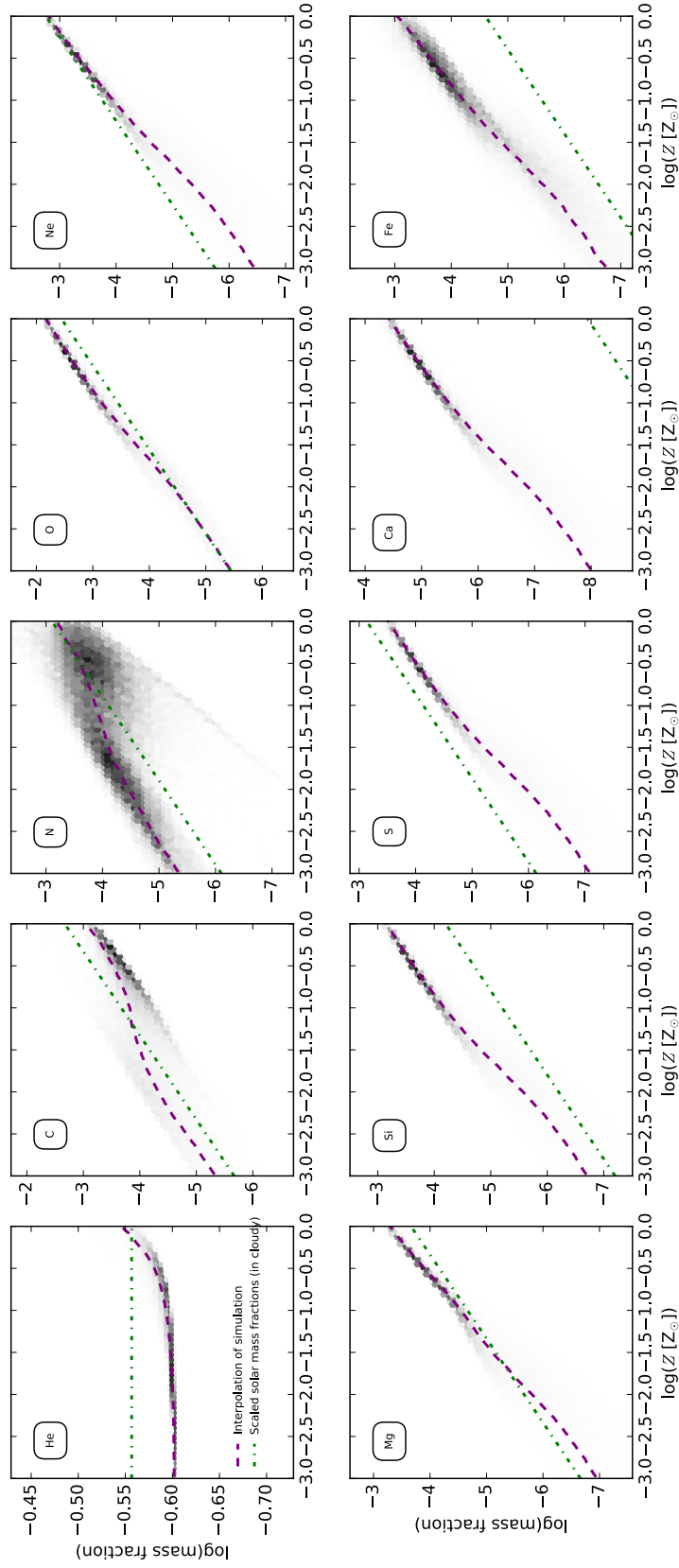


Figure 12. Grey contours represent the mass fractions of the elements tracked in the MUFASA simulation set as function of the metallicity of individual fluid elements for a subsample of three randomly selected model galaxies used in this work. Using the local ISM abundances stored in CLOUDY and scaled by metallicity gives the green dash-dotted line. These are our default abundances in SÍGAME for this project. We also make a grid of cloudy models in which each element shown here is scaled to match the simulation as represented by the purple dashed lines which consist of running means of the values of the gas fluid elements.

findings at face value would suggest that the [C II]-bright LBGs may have higher fractions of either ionized or molecular gas, or both, than our simulations and [C II]-faint sources.

To investigate this we first show in Fig. 13 the molecular gas mass fractions (f_{mol}) of our simulated galaxies as calculated directly from Table 1. The molecular gas mass fractions decrease with SFR, going from ~ 0.6 at the lowest SFR to ~ 0.1 at the highest SFRs (red filled circles in Fig. 13). For the Capak et al. (2015) and Willott et al. (2015) LBGs we do not have direct estimates of their gas mass fractions. Instead we apply to them the parametrisations provided by Scoville et al. (2016), which give f_{mol} as a function of z , M_* , and SFR (and denominated $f_{\text{mol},\text{S16}}$ in the figure). The resulting fractions for the LBGs, shown as green diamonds and crosses in Fig. 13, are significantly higher ($f_{\text{mol},\text{S16}} \sim 0.4 - 0.6$) than those of our simulations at $\text{SFR} \gtrsim 10 M_\odot \text{ yr}^{-1}$ ($f_{\text{mol}} \sim 0.1$). Applying the same parametrisations to our simulated galaxies yields $f_{\text{mol},\text{S16}} \sim 0.4$, which matches well with the Capak et al. (2015) and Willott et al. (2015) sources. This would mean roughly $4\times$ higher f_{mol} at the highest SFRs of our models, which translates into a $6\times$ higher molecular gas mass for a fixed stellar mass. For comparison we also show the ionized gas mass fractions, f_{ion} , of our model galaxies, which at present cannot be compared to the $z \sim 5 - 6$ LBGs of Capak et al. (2015) and Willott et al. (2015), but we note a decrease in f_{ion} with SFR similar to that of f_{mol} .

In adopting the relation from Scoville et al. (2016), we are making three major assumptions: 1) that the relation created from galaxies out to $z = 5.89$ can be extrapolated to $z \sim 6$, 2) that M_* and SFR are derived in similar fashions from observations as from our simulations, and 3) that the actual molecular gas masses in our simulations correspond to the dust-derived molecular ISM masses used in Scoville et al. (2016). However, if all these assumptions are valid, then it implies that the range of f_{mol} in our model galaxies does not reach the higher f_{mol} values derived for observed galaxies close to $z = 6$. This will tend to make our models underpredict the [C II] emission since we find that the [C II] efficiency of molecular regions is generally higher than diffuse regions of the ISM (cf. Fig 7).

Metallicities. In §4.4 we saw that simulations with higher average metallicities also tend to have higher [C II] luminosities (Fig. 9 and eq. 11). Our simulations all have metallicities well below solar ($\langle Z \rangle_{\text{SFR}} \lesssim 0.45$) – and less than half the metallicity of the local metal-poor dwarf galaxies studied by De Looze et al. (2014) – which may therefore partly account for their [C II] faint-

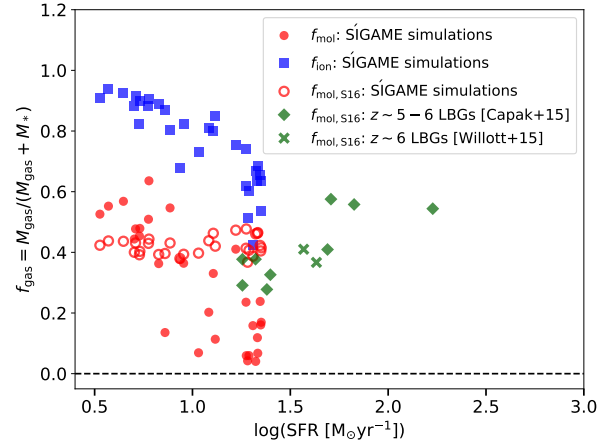


Figure 13. Molecular gas mass fractions of our simulations and of the $z \sim 5 - 6$ LBGs observed by Capak et al. (2015) and Willott et al. (2015). The filled and open red circles indicate true fractions inferred directly from the simulations and fractions inferred from the parametrisations in Scoville et al. (2016), respectively. Applying this parametrisation to the $z \sim 5 - 6$ LBGs gives the molecular gas mass fractions shown by the green diamonds and crosses. Also shown are the true ionized gas mass fraction of our simulations (blue filled squares).

ness and the discrepancy with the Capak et al. (2015) sources which are likely to have higher metallicities.

Fig. 14 shows the [C II]-SFR relation obtained when scaling the metallicities of our simulations by a factor of three leading to SFR-weighted metallicities of 0.4 to 1.4 solar and a mass-metallicity relation for our model galaxies close to that observed at $z \sim 1.3 - 2.3$ for galaxies of similar masses (Erb et al. 2006; Henry et al. 2013; Sanders et al. 2015). This is therefore an extreme case, in which our $z \sim 6$ galaxies have already achieved typical metallicities at $z \sim 1.3 - 2.3$. In order to test this case, new CLOUDY grids were calculated for both the dense and diffuse gas. The net effect of raising the metallicities is to increase the [C II] luminosities of our simulations by 0.4 dex on average, thereby bringing them better in line with the [C II] detections of Capak et al. (2015) at $\text{SFR} \sim 20 M_\odot \text{ yr}^{-1}$. This picture is consistent with the relatively low Ly α line strength measured for the $z \sim 5 - 6$ detections (Capak et al. 2015; Willott et al. 2015; Pentericci et al. 2016), since the Ly α strength decreases with the dust amount and hence metallicity (e.g. Pirzkal et al. 2007; Yang et al. 2017), except in cases where the ISM is very inhomogeneous (e.g. Giallisco et al. 1996), though see also the model results by Laursen et al. (2013).

We note that the ~ 0.4 dex increase in [C II] luminosity of our simulations is mainly coming from the neutral and

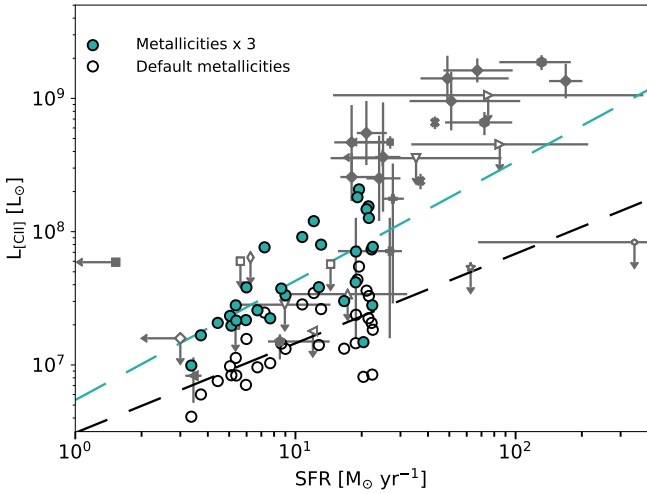


Figure 14. The effect of boosting the (default) metallicities of each fluid element in our simulations by a factor of three results in galaxy [C II] luminosities (filled cyan circles) that are on average $\sim 2.5 - 3\times$ higher. Even so, this does not bring the simulations fully into accord with the [C II]-bright detections at $z \simeq 6$, although there is an overlap with observations for some simulations. The dashed cyan line shows the log-linear fit to the simulations with high metallicities.

diffuse ionized gas where an increase in the metallicity results in a higher abundance of C^+ . For the GMCs, an increase in the metallicity results in a higher degree of UV-attenuation by dust and therefore thinner C^+ layers. This is the same effect we saw in Fig. 7 where the fraction of the total [C II] luminosity coming from GMCs decreases with increasing metallicity of the simulations.

6. CONCLUSION

We have applied an updated version of SÍGAME to MUFASA simulations in order to model the [C II], [O I], and [O III] line emission from $z \sim 6$ galaxies on the main sequence with stellar masses $\sim (0.7 - 8) \times 10^9 M_\odot$ and metallicities $\sim (0.1 - 0.4) \times Z_\odot$.

The simulations are able to reproduce observations of [C II]-faint star forming galaxies at $z \gtrsim 5$ – i.e., galaxies with [C II] luminosities (many of which are upper limits) that are $\sim 6 - 32\times$ lower than expected from local $L_{[C II]}$ -SFR relations and from samples of [C II]-bright galaxies at $z \sim 5 - 6$ (Capak et al. 2015; Willott et al. 2015). Extrapolating a log-linear fit to our simulations to higher SFRs ($\sim 50 - 300 M_\odot \text{ yr}^{-1}$) results in agreement with observations of [C II]-faint galaxies at these higher SFRs.

The [O I] and [O III] luminosities from the simulated galaxies are in broad agreement with the $L_{[O I]}$ -SFR and $L_{[O III]}$ -SFR relations of local starburst galaxies (De Looze et al. 2014), as well as with two of the three exist-

ing $z \gtrsim 5$ detections of [O III] to date (Inoue et al. 2016; Laporte et al. 2017).

Dividing the [C II] luminosities of our simulations into contributions from the different ISM phases, we find that the [C II] emission predominantly comes from the diffuse ionized gas and the GMCs, which on average contribute by $\sim 66\%$ and $\sim 27\%$, respectively, while the diffuse neutral phase contributes by $\sim 7\%$. In terms of mass, the three phases constitute on average $\sim 85\%$, $\sim 10\%$, and $\sim 10\%$ of the total ISM mass in our simulations. Thus, the GMCs are the most efficient [C II] emitters of the ISM phases, suggesting that the molecular gas fraction plays a role in whether a galaxy is [C II]-faint or [C II]-bright.

A principle component analysis shows that $L_{[C II]}$ primarily depends on Σ_{SFR} and SFR. Furthermore, including metallicity in the set of free global parameters reduces the scatter between $L_{[C II]}$ from the PCA parametrization and $L_{[C II]}$ from the simulations. In our models, the ISM mass is not an important parameter in setting $L_{[C II]}$.

The modeling presented in this paper suggest that the [C II]-faint $z \gtrsim 5$ main sequence galaxies, including [C II] non-detections, are likely the result of low metallicities and low molecular gas fractions. More observations of FIR emission lines at high redshift together with more precise SFR determinations are needed in order to compare better with models such as ours, yet at the same time we have to work towards modeling galaxies with more dynamic range in physical parameters such as metallicity and SFR.

ACKNOWLEDGMENTS

The authors thank the anonymous referee for a careful reading of the manuscript and insightful comments that greatly improved the quality of this work. The authors thank Sangeeta Malhotra and Kristian Finlator for fruitful discussion. The authors acknowledge the Texas Advanced Computing Center (TACC) at The University of Texas at Austin for providing high performance computing resources that have contributed to the research results reported within this paper (<http://www.tacc.utexas.edu>). In addition, this work benefited from resources provided by the NASA High-End Computing (HEC) Program through the NASA Advanced Supercomputing (NAS) Division, and from computational resources and technical expertise provided by ASU Research Computing, Tempe, Arizona. The hydrodynamic simulations published here were run on the University of Florida HiPerGator facility, and the authors acknowledge the University of Florida Research Computing for providing computational resources and

support that have contributed to the research results reported in this publication. Partial support for DN was provided by NSF AST-1009452, AST-1445357, NASA HST AR-13906.001 from the Space Telescope Science

Institute, which is operated by the Association of University for Research in Astronomy, Incorporated, under NASA Contract NAS5-26555, and a Cottrell College Science Award, awarded by the Research Corporation for Science Advancement.

REFERENCES

- Accurso, G., Saintonge, A., Bisbas, T. G., & Viti, S. 2017, *MNRAS*, 464, 3315
- Asplund, M., Grevesse, N., Sauval, A. J., & Scott, P. 2009, *ARA&A*, 47, 481
- Blitz, L., Fukui, Y., Kawamura, A., et al. 2007, *Protostars and Planets V*, 81
- Bonato, M., Negrello, M., Cai, Z.-Y., et al. 2014, *MNRAS*, 438, 2547
- Bradač, M., Garcia-Appadoo, D., Huang, K.-H., et al. 2017, *ApJL*, 836, L2
- Brauher, J. R., Dale, D. A., & Helou, G. 2008, *ApJS*, 178, 280
- Bruzual, G., & Charlot, S. 2003, *MNRAS*, 344, 1000
- Capak, P. L., Carilli, C., Jones, G., et al. 2015, *Nature*, 522, 455
- Carniani, S., Maiolino, R., Pallottini, A., et al. 2017, *ArXiv e-prints*, arXiv:1701.03468
- Chabrier, G. 2003, *PASP*, 115, 763
- Chomiuk, L., & Povich, M. S. 2011, *AJ*, 142, 197
- Conroy, C., Gunn, J. E., & White, M. 2009, *ApJ*, 699, 486
- Conroy, C., White, M., & Gunn, J. E. 2010, *ApJ*, 708, 58
- Cormier, D., Leboutteiller, V., Madden, S. C., et al. 2012, *A&A*, 548, A20
- Davé, R., Rafieferantsoa, M. H., Thompson, R. J., & Hopkins, P. F. 2017, *MNRAS*, 467, 115
- Davé, R., Thompson, R., & Hopkins, P. F. 2016, *MNRAS*, 462, 3265
- De Cia, A., Ledoux, C., Mattsson, L., et al. 2016, *A&A*, 596, A97
- De Cia, A., Ledoux, C., Savaglio, S., Schady, P., & Vreeswijk, P. M. 2013, *A&A*, 560, A88
- De Looze, I., Cormier, D., Leboutteiller, V., et al. 2014, *A&A*, 568, A62
- Decarli, R., Walter, F., Venemans, B. P., et al. 2017, *Nature*, 545, 457
- Díaz-Santos, T., Armus, L., Charmandaris, V., et al. 2013, *ApJ*, 774, 68
- Díaz-Santos, T., Armus, L., Charmandaris, V., et al. 2017, *ArXiv e-prints*, arXiv:1705.04326
- Draine, B. T. 2011, *Physics of the Interstellar and Intergalactic Medium*
- Erb, D. K., Shapley, A. E., Pettini, M., et al. 2006, *ApJ*, 644, 813
- Ferkinhoff, C., Hailey-Dunsheath, S., Nikola, T., et al. 2010, *ApJL*, 714, L147
- Ferland, G. J., Porter, R. L., van Hoof, P. A. M., et al. 2013, *RxMAA*, 49, 137
- Ferland, G. J., Chatzikos, M., Guzmán, F., et al. 2017, *ArXiv e-prints*, arXiv:1705.10877
- Fischer, J., Luhman, M. L., Satyapal, S., et al. 1999, *Ap&SS*, 266, 91
- Giavalisco, M., Koratkar, A., & Calzetti, D. 1996, *ApJ*, 466, 831
- Goldsmith, P. F., Langer, W. D., Pineda, J. L., & Velusamy, T. 2012, *ApJS*, 203, 13
- González-López, J., Riechers, D. A., Decarli, R., et al. 2014, *ApJ*, 784, 99
- Gullberg, B., De Breuck, C., Vieira, J. D., et al. 2015, *MNRAS*, 449, 2883
- Hahn, O., & Abel, T. 2011, *MNRAS*, 415, 2101
- Hayward, C. C., & Smith, D. J. B. 2015, *MNRAS*, 446, 1512
- Helou, G., Malhotra, S., Hollenbach, D. J., Dale, D. A., & Contursi, A. 2001, *ApJL*, 548, L73
- Henry, A., Scarlata, C., Domínguez, A., et al. 2013, *ApJL*, 776, L27
- Herrera-Camus, R., Bolatto, A. D., Wolfire, M. G., et al. 2015, *ApJ*, 800, 1
- Hopkins, P. F. 2015, *MNRAS*, 450, 53
- Inoue, A. K., Tamura, Y., Matsuo, H., et al. 2016, *Science*, 352, 1559
- Iwamoto, K., Brachwitz, F., Nomoto, K., et al. 1999, *ApJS*, 125, 439
- Jiang, L., Finlator, K., Cohen, S. H., et al. 2016, *ApJ*, 816, 16
- Jolliffe, I. 2002, *Principal component analysis* (New York: Springer Verlag)
- Kanekar, N., Wagg, J., Ram Chary, R., & Carilli, C. L. 2013, *ApJL*, 771, L20
- Kapala, M. J., Sandstrom, K., Groves, B., et al. 2015, *ApJ*, 798, 24
- Katz, H., Kimm, T., Sijacki, D., & Haehnelt, M. G. 2017, *MNRAS*, 468, 4831

- Kennicutt, R. C., & Evans, N. J. 2012, *ARA&A*, 50, 531
- Knudsen, K. K., Richard, J., Kneib, J.-P., et al. 2016, *MNRAS*, 462, L6
- Knudsen, K. K., Watson, D., Frayer, D., et al. 2017, *MNRAS*, 466, 138
- Krumholz, M. R., & Gnedin, N. Y. 2011, *ApJ*, 729, 36
- Krumholz, M. R., McKee, C. F., & Tumlinson, J. 2009, *ApJ*, 693, 216
- Laporte, N., Ellis, R. S., Boone, F., et al. 2017, *ApJL*, 837, L21
- Laursen, P., Duval, F., & Östlin, G. 2013, *ApJ*, 766, 124
- Leitherer, C., Ekström, S., Meynet, G., et al. 2014, *ApJS*, 212, 14
- Luhman, M. L., Satyapal, S., Fischer, J., et al. 2003, *ApJ*, 594, 758
- . 1998, *ApJL*, 504, L11
- Maiolino, R., Cox, P., Caselli, P., et al. 2005, *A&A*, 440, L51
- Maiolino, R., Carniani, S., Fontana, A., et al. 2015, *MNRAS*, 452, 54
- Malhotra, S., Helou, G., Stacey, G., et al. 1997, *ApJL*, 491, L27
- Malhotra, S., Kaufman, M. J., Hollenbach, D., et al. 2001, *ApJ*, 561, 766
- Muñoz, J. A., & Furlanetto, S. R. 2014, *MNRAS*, 438, 2483
- Muratov, A. L., Kereš, D., Faucher-Giguère, C.-A., et al. 2015, *MNRAS*, 454, 2691
- Narayanan, D., Dave, R., Johnson, B., et al. 2017, *arXiv/1705.05858*, *arXiv:1705.05858*
- Narayanan, D., Krumholz, M., Ostriker, E. C., & Hernquist, L. 2011, *MNRAS*, 418, 664
- Narayanan, D., & Krumholz, M. R. 2017, *MNRAS*, 467, 50
- Narayanan, D., Dey, A., Hayward, C. C., et al. 2010, *MNRAS*, 407, 1701
- Narayanan, D., Turk, M., Feldmann, R., et al. 2015, *Nature*, 525, 496
- Nomoto, K., Tominaga, N., Umeda, H., Kobayashi, C., & Maeda, K. 2006, *Nuclear Physics A*, 777, 424
- Olsen, K. P., Greve, T. R., Narayanan, D., et al. 2015, *ApJ*, 814, 76
- Oppenheimer, B. D., & Davé, R. 2008, *MNRAS*, 387, 577
- Ota, K., Walter, F., Ohta, K., et al. 2014, *ApJ*, 792, 34
- Ouchi, M., Ellis, R., Ono, Y., et al. 2013, *ApJ*, 778, 102
- Pallottini, A., Ferrara, A., Gallerani, S., et al. 2017, *MNRAS*, 465, 2540
- Papadopoulos, P. P., Thi, W.-F., Miniati, F., & Viti, S. 2011, *MNRAS*, 414, 1705
- Papadopoulos, P. P., Zhang, Z.-Y., Xilouris, E. M., et al. 2014, *ApJ*, 788, 153
- Pentericci, L., Carniani, S., Castellano, M., et al. 2016, *ApJL*, 829, L11
- Pineda, J. L., Langer, W. D., & Goldsmith, P. F. 2014, *A&A*, 570, A121
- Pirzkal, N., Malhotra, S., Rhoads, J. E., & Xu, C. 2007, *ApJ*, 667, 49
- Planck Collaboration, Ade, P. A. R., Aghanim, N., et al. 2016, *A&A*, 594, A13
- Popping, G., van Kampen, E., Decarli, R., et al. 2016, *MNRAS*, 461, 93
- Rahmati, A., Pawlik, A. H., Raičević, M., & Schaye, J. 2013, *MNRAS*, 430, 2427
- Rigopoulou, D., Hopwood, R., Magdis, G. E., et al. 2014, *ApJL*, 781, L15
- Robitaille, T. P. 2011, *A&A*, 536, A79
- Robitaille, T. P., Churchwell, E., Benjamin, R. A., et al. 2012, *A&A*, 545, A39
- Röllig, M., Ossenkopf, V., Jeyakumar, S., Stutzki, J., & Sternberg, A. 2006, *A&A*, 451, 917
- Rosenberg, M. J. F., van der Werf, P. P., Aalto, S., et al. 2015, *ApJ*, 801, 72
- Rosolowsky, E. 2005, *PASP*, 117, 1403
- Sanders, R. L., Shapley, A. E., Kriek, M., et al. 2015, *ApJ*, 799, 138
- Sargsyan, L., Samsonyan, A., Leboutteiller, V., et al. 2014, *ApJ*, 790, 15
- Schaerer, D., Boone, F., Zamojski, M., et al. 2015, *A&A*, 574, A19
- Schmidt, M. 1959, *ApJ*, 129, 243
- Scoville, N., Sheth, K., Aussel, H., et al. 2016, *ApJ*, 820, 83
- Seon, K.-I., Edelman, J., Korpela, E., et al. 2011, *ApJS*, 196, 15
- Smit, R., Bouwens, R. J., Carniani, S., et al. 2017, *ArXiv e-prints*, *arXiv:1706.04614*
- Smith, J. D. T., Croxall, K., Draine, B., et al. 2017, *ApJ*, 834, 5
- Somerville, R. S., & Davé, R. 2015, *ARA&A*, 53, 51
- Speagle, J. S., Steinhardt, C. L., Capak, P. L., & Silverman, J. D. 2014, *ApJS*, 214, 15
- Springel, V. 2005, *MNRAS*, 364, 1105
- Stacey, G. J., Geis, N., Genzel, R., et al. 1991, *ApJ*, 373, 423
- Stacey, G. J., Hailey-Dunsheath, S., Ferkinhoff, C., et al. 2010, *ApJ*, 724, 957
- Sturm, E., Verma, A., Graciá-Carpio, J., et al. 2010, *A&A*, 518, L36
- Turk, M. J., Smith, B. D., Oishi, J. S., et al. 2011, *ApJS*, 192, 9
- Vallini, L., Gallerani, S., Ferrara, A., & Baek, S. 2013, *MNRAS*, 433, 1567

- Vallini, L., Gallerani, S., Ferrara, A., Pallottini, A., & Yue, B. 2015, *ApJ*, 813, 36
- Venemans, B. P., McMahon, R. G., Walter, F., et al. 2012, *ApJL*, 751, L25
- Vladilo, G. 2004, *A&A*, 421, 479
- Wang, R., Wagg, J., Carilli, C. L., et al. 2013a, *ApJ*, 773, 44
- . 2013b, *ApJ*, 773, 44
- Webber, W. R. 1998, *ApJ*, 506, 329
- Willott, C. J., Carilli, C. L., Wagg, J., & Wang, R. 2015, *ApJ*, 807, 180
- Willott, C. J., Omont, A., & Bergeron, J. 2013, *ApJ*, 770, 13
- Wiseman, P., Schady, P., Bolmer, J., et al. 2017, *A&A*, 599, A24
- Yang, H., Malhotra, S., Gronke, M., et al. 2017, *ArXiv e-prints*, arXiv:1701.01857
- Zhao, Y., Yan, L., & Tsai, C.-W. 2016, *ApJ*, 824, 146